

1      **High-level cognition during story listening is reflected in  
2      high-order dynamic correlations in neural activity patterns**

3      Lucy L. W. Owen<sup>1</sup>, Thomas H. Chang<sup>1,2</sup>, and Jeremy R. Manning<sup>1,†</sup>

<sup>1</sup>Department of Psychological and Brain Sciences,  
Dartmouth College, Hanover, NH

<sup>2</sup>Amazon.com, Seattle, WA

†Address correspondence to jeremy.r.manning@dartmouth.edu

4      July 2, 2021

5      **Abstract**

6      Our thoughts arise from coordinated patterns of interactions between brain structures that change  
7      with our ongoing experiences. High-order dynamic correlations in neural activity patterns reflect different  
8      subgraphs of the brain’s functional connectome that display homologous lower-level dynamic correlations.  
9      Here we test the hypothesis that high-level cognition is reflected in high-order dynamic correlations in brain  
10     activity patterns. We develop an approach to estimating high-order dynamic correlations in timeseries data,  
11     and we apply the approach to neuroimaging data collected as human participants either listen to a ten-  
12     minute story or listen to a temporally scrambled version of the story. We train across-participant pattern  
13     classifiers to decode (in held-out data) when in the session each neural activity snapshot was collected. We  
14     find that classifiers trained to decode from high-order dynamic correlations yield the best performance on  
15     data collected as participants listened to the (unscrambled) story. By contrast, classifiers trained to decode  
16     data from scrambled versions of the story yielded the best performance when they were trained using first-  
17     order dynamic correlations or non-correlational activity patterns. We suggest that as our thoughts become  
18     more complex, they are reflected in higher-order patterns of dynamic network interactions throughout the  
19     brain.

20     **Introduction**

21     A central goal in cognitive neuroscience is to elucidate the neural code: the mapping between (a) mental  
22     states or cognitive representations and (b) neural activity patterns. One means of testing models of the  
23     neural code is to ask how accurately that model is able to “translate” neural activity patterns into known  
24     (or hypothesized) mental states or cognitive representations e.g.,<sup>1–9</sup>. Training decoding models on different  
25     types of neural features (Fig. 1a) can also help to elucidate which specific aspects of neural activity patterns  
26     are informative about cognition and, by extension, which types of neural activity patterns might compose  
27     the neural code. For example, prior work has used region of interest analyses to estimate the anatomical  
28     locations of specific neural representations e.g.,<sup>10</sup>, or to compare the relative contributions to the neural  
29     code of multivariate activity patterns versus dynamic correlations between neural activity patterns e.g.,<sup>11,12</sup>.

30 An emerging theme in this literature is that cognition is mediated by dynamic interactions between brain  
31 structures<sup>13–25</sup>.

32 [Figure 1 about here.]

33 Studies of the neural code to date have primarily focused on univariate or multivariate neural patterns for  
34 review see<sup>2</sup>, or (more recently) on patterns of dynamic first-order correlations i.e., interactions between pairs  
35 of brain structures;<sup>11,12,18,20–22</sup>. What might the future of this line of work hold? For example, is the neural  
36 code implemented through higher-order interactions between brain structures e.g., see<sup>26</sup>? Second-order  
37 correlations reflect homologous patterns of correlation. In other words, if the dynamic patterns of correla-  
38 tions between two regions, *A* and *B*, are similar to those between two other regions, *C* and *D*, this would  
39 be reflected in the second-order correlations between (*A*-*B*) and (*C*-*D*). In this way, second-order corre-  
40 lations identify similarities and differences between subgraphs of the brain’s connectome. Analogously,  
41 third-order correlations reflect homologies between second-order correlations—i.e., homologous patterns of  
42 homologous interactions between brain regions. More generally, higher-order correlations reflect homolo-  
43 gies between patterns of lower-order correlations. We can then ask: which “orders” of interaction are most  
44 reflective of high-level cognitive processes?

45 One reason one might expect to see homologous networks in a dataset is related to the notion that network  
46 dynamics reflect ongoing neural computations or cognitive processing e.g.,<sup>27</sup>. If the nodes in two brain  
47 networks are interacting (within each network) in similar ways then, according to our characterization  
48 of network dynamics, we refer to the similarities between those patterns of interaction as higher-order  
49 correlations. When higher-order correlations are themselves changing over time, we can also attempt to  
50 capture and characterize those high-order dynamics.

51 Another central question pertains to the extent to which the neural code is carried by activity patterns that  
52 directly reflect ongoing cognition e.g., following<sup>1,2</sup>, versus the dynamic properties of the network structure  
53 itself, independent of specific activity patterns in any given set of regions e.g., following<sup>16</sup>. For example,  
54 graph measures such as centrality and degree<sup>28</sup> may be used to estimate how a given brain structure is  
55 “communicating” with other structures, independently of the specific neural representations carried by  
56 those structures. If one considers a brain region’s position in the network (e.g., its eigenvector centrality) as  
57 a dynamic property, one can compare how the positions of different regions are correlated, and/or how those  
58 patterns of correlations change over time. We can also compute higher-order patterns in these correlations  
59 to characterize homologous subgraphs in the connectome that display similar changes in their constituent  
60 brain structures’ interactions with the rest of the brain.

61 To gain insights into the above aspects of the neural code, we developed a computational framework

62 for estimating dynamic high-order correlations in timeseries data. This framework provides an important  
63 advance, in that it enables us to examine patterns of higher-order correlations that are computationally  
64 intractable to estimate via conventional methods. Given a multivariate timeseries, our framework pro-  
65 vides timepoint-by-timepoint estimates of the first-order correlations, second-order correlations, and so  
66 on. Our approach combines a kernel-based method for computing dynamic correlations in timeseries  
67 data with a dimensionality reduction step (Fig. 1b) that projects the resulting dynamic correlations into  
68 a low-dimensional space. We explored two dimensionality reduction approaches: principle components  
69 analysis PCA,<sup>29</sup>, which preserves an approximately invertible transformation back to the original data e.g.,  
70 this follows related approaches taken by<sup>30–32</sup>; and a second non-invertible algorithm for computing dy-  
71 namic patterns in eigenvector centrality<sup>33</sup>. This latter approach characterizes correlations between each  
72 feature dimension’s relative position in the network (at each moment in time) in favor of the specific activity  
73 histories of different features also see<sup>26,34,35</sup>.

74 We validated our approach using synthetic data where the underlying correlations were known. We  
75 then applied our framework to a neuroimaging dataset collected as participants listened to either an audio  
76 recording of a ten-minute story, listened to a temporally scrambled version of the story, or underwent a  
77 resting state scan<sup>36</sup>. Temporal scrambling has been used in a growing number of studies, largely by Uri  
78 Hasson’s group, to identify brain regions that are sensitive to higher-order and longer-timescale information  
79 (e.g., cross-sensory integration, rich narrative meaning, complex situations, etc.) versus regions that are  
80 primarily sensitive to low-order (e.g., sensory) information. For example,<sup>37</sup> argues that when brain areas  
81 are sensitive to fine versus coarse temporal scrambling, this indicates that they are “higher order” in the  
82 sense that they process contextual information pertaining to further-away timepoints. By contrast, low-level  
83 regions, such as primary sensory cortices, do not meaningfully change their responses (after correcting for  
84 presentation order) even when the stimulus is scrambled at fine timescales.

85 We used a subset of the story listening and rest data to train across-participant classifiers to decode  
86 listening times (of groups of participants) using a blend of neural features (comprising neural activity  
87 patterns, as well as different orders of dynamic correlations between those patterns that were inferred  
88 using our computational framework). We found that both the PCA-based and eigenvector centrality-based  
89 approaches yielded neural patterns that could be used to decode accurately (i.e., well above chance). Both  
90 approaches also yielded the best decoding accuracy for data collected during (intact) story listening when  
91 high-order (PCA: second-order; eigenvector centrality: fourth-order) dynamic correlation patterns were  
92 included as features. When we trained classifiers on the scrambled stories or resting state data, only  
93 (relatively) lower-order dynamic patterns were informative to the decoders. Taken together, our results  
94 indicate that high-level cognition is supported by high-order dynamic patterns of communication between

95 brain structures.

## 96 Results

97 We sought to understand whether high-level cognition is reflected in dynamic patterns of high-order correla-  
98 tions. To that end, we developed a computational framework for estimating the dynamics of stimulus-driven  
99 high-order correlations in multivariate timeseries data (see Dynamic inter-subject functional connectivity  
100 (DISFC) and Dynamic higher-order correlations). We evaluated the efficacy of this framework at recovering  
101 known patterns in several synthetic datasets (see Synthetic data: simulating dynamic first-order corre-  
102 lations and Synthetic data: simulating dynamic higher-order correlations). We then applied the framework  
103 to a public fMRI dataset collected as participants listened to an auditorily presented story, listened to a  
104 temporally scrambled version of the story, or underwent a resting state scan (see Functional neuroimaging  
105 data collected during story listening). We used the relative decoding accuracies of classifiers trained on  
106 different sets of neural features to estimate which types of features reflected ongoing cognitive processing.

### 107 Recovering dynamic first-order correlations

108 We generated synthetic datasets that differed in how the underlying first-order correlations changed over  
109 time. For each dataset, we applied Equation 4 with a variety of kernel shapes and widths. We assessed how  
110 well the true underlying correlations at each timepoint matched the recovered correlations (Fig. 2). For every  
111 kernel and dataset we tested, our approach recovered the correlation dynamics we embedded into the data.  
112 However, the quality of these recoveries varied across different synthetic datasets in a kernel-dependent  
113 way.

114 [Figure 2 about here.]

115 In general, wide monotonic kernel shapes (Laplace, Gaussian), and wider kernels (within a shape),  
116 performed best when the correlations varied gradually from moment-to-moment (Figs. 2a, c, and d). In the  
117 extreme, as the rate of change in correlations approaches 0 (Fig. 2a), an infinitely wide kernel would exactly  
118 recover the Pearson's correlation (e.g., compare Eqns. 1 and 4).

119 When the correlation dynamics were unstructured in time (Fig. 2b), a Dirac  $\delta$  kernel (infinitely narrow)  
120 performed best. This is because, when every timepoint's correlations are independent of the correlations at  
121 every other timepoint, averaging data over time dilutes the available signal. Following a similar pattern,  
122 holding kernel shape fixed, narrower kernel parameters better recovered randomly varying correlations.

123 **Recovering dynamic higher-order correlations**

124 Following our approach to evaluating our ability to recover known dynamic first-order correlations from  
125 synthetic data, we generated an analogous second set of synthetic datasets that we designed to exhibit  
126 known dynamic first-order and second-order correlations (see Synthetic data: simulating dynamic higher-  
127 order correlations). We generated a total of 400 datasets (100 datasets for each category) that varied in how  
128 the first-order and second-order correlations changed over time. We then repeatedly applied Equation 4  
129 using the overall best-performing kernel from our first-order tests (a Laplace kernel with a width of 20;  
130 Fig. 2) to assess how closely the recovered dynamic correlations matched the dynamic correlations we had  
131 embedded into the datasets.

132 Overall, we found that we could reliably recover both first-order and second-order correlations from the  
133 synthetic data (Fig. 3). When the correlations were stable for longer intervals, or changed gradually (constant,  
134 ramping, and event datasets), recovery performance was relatively high, and we were better able to recover  
135 dynamic first-order correlations than second-order correlations. This is because errors in our estimation  
136 procedure at lower orders necessarily propagate to higher orders (since lower-order correlations are used to  
137 estimate higher-order correlations). Conversely, when the correlations were particularly unstable (random  
138 datasets), we better recovered second-order correlations. This is because noises in our data generation  
139 procedure propagates from higher orders to lower orders (see Synthetic data: simulating dynamic high-  
140 order correlations).

141 [Figure 3 about here.]

142 We also examined the impact of the data duration (Fig. S3) and complexity (number of zero-order features;  
143 Fig. S4) on our ability to accurately recover ground truth first-order and second-order dynamic correlations.  
144 In general, we found that our approach better recovers ground truth dynamic correlations from longer  
145 duration timeseries data. We also found that our approach tends to best recover data generated using fewer  
146 zero-order features (i.e., lower complexity), although this tendency was not strictly monotonic. Further,  
147 because our data generation procedure requires  $O(K^4)$  memory to generate a second-order timeseries with  $K$   
148 zero-order features, we were not able to fully explore how the number of zero-order features affects recovery  
149 accuracy as the number of features gets larger (e.g., as it approaches the number of features present in the  
150 fMRI data we examine below). Although we were not able to formally test this to our satisfaction, we expect  
151 that accurately estimating dynamic high-order correlations would require data with many more zero-order  
152 features than we were able to simulate. Our reasoning is that high-order correlations necessarily involve  
153 larger numbers of lower-order features, so achieving adequate “resolution” high-order timeseries might  
154 require many low-order features.

155 Taken together, our explorations using synthetic data indicated that we are able to partially, but not  
156 perfectly, recover ground truth dynamic first-order and second-order correlations. This suggests that our  
157 modeling approach provides a meaningful (if noisy) estimate of high-order correlations. We next turned  
158 to analyses of human fMRI data to examine whether the recovered dynamics might reflect the dynamics of  
159 human cognition during a naturalistic story-listening task.

160 **Cognitively relevant dynamic high-order correlations in fMRI data**

161 We used across-participant temporal decoders to identify cognitively relevant neural patterns in fMRI data  
162 (see Forward inference and decoding accuracy). The dataset we examined collected by<sup>36</sup> comprised four  
163 experimental conditions that exposed participants to stimuli that varied systematically in how cognitively  
164 engaging they were. The intact experimental condition had participants listen to an audio recording of a  
165 10-minute story. The paragraph-scrambled experimental condition had participants listen to a temporally  
166 scrambled version of the story, where the paragraphs occurred out of order (but where the same total set of  
167 paragraphs were presented over the full listening interval). All participants in this condition experienced  
168 the scrambled paragraphs in the same order. The word-scrambled experimental condition had participants  
169 listen to a temporally scrambled version of the story where the words in the story occurred in a random  
170 order. All participants in the word condition experienced the scrambled words in the same order. Finally,  
171 in a rest experimental condition, participants lay in the scanner with no overt stimulus, with their eyes  
172 open (blinking as needed). This public dataset provided a convenient means of testing our hypothesis that  
173 different levels of cognitive processing and engagement are reflected in different orders of brain activity  
174 dynamics.

175 [Figure 4 about here.]

176 In brief, we computed timeseries of dynamic high-order correlations that were similar across participants  
177 in each of two randomly assigned groups: a training group and a test group. We then trained classifiers  
178 on the training group's data to match each sample from the test group with a stimulus timepoint. Each  
179 classifier comprised a weighted blend of neural patterns that reflected up to  $n^{\text{th}}$ -order dynamic correlations  
180 (see Feature weighting and testing, Fig. 10). We repeated this process for  $n \in \{0, 1, 2, \dots, 10\}$ . Our examinations  
181 of synthetic data suggested that none of the kernels we examined were “universal” in the sense of optimally  
182 recovering underlying correlations regardless of the temporal structure of those correlations. We found a  
183 similar pattern in the (real) fMRI data, whereby different kernels yielded different decoding accuracies, but  
184 no single kernel emerged as the clear “best.” In our analyses of neural data, we therefore averaged our

185 decoding results over a variety of kernel shapes and widths in order to identify results that were robust to  
186 specific kernel parameters (see Identifying robust decoding results).

187 Our approach to estimating dynamic high-order correlations entails mapping the high-dimensional  
188 feature space of correlations (represented by a  $T$  by  $O(K^2)$  matrix) onto a lower-dimensional feature space  
189 (represented by a  $T$  by  $K$  matrix). We carried out two sets of analyses that differed in how this mapping was  
190 computed. The first set of analyses used PCA to find a low-dimensional embedding of the original dynamic  
191 correlation matrices (Fig. 4a,b). The second set of analyses characterized correlations in dynamics of each  
192 feature's eigenvector centrality, but did not preserve the underlying activity dynamics (Fig. 4c,d).

193 [Figure 5 about here.]

194 Both sets of temporal decoding analyses yielded qualitatively similar results for the auditory (non-rest)  
195 conditions of the experiment (Fig. 4: pink, green, and teal lines; Fig. 5: three leftmost columns). The highest  
196 decoding accuracy for participants who listened to the intact (unscrambled) story was achieved using high-  
197 order dynamic correlations (PCA: second-order; eigenvector-centrality: fourth-order). Scrambled versions  
198 of the story were best decoded by lower-order correlations (PCA/paragraph: first-order; PCA/word: order  
199 zero; eigenvector centrality/paragraph: order zero; eigenvector centrality/word: order zero). The two sets  
200 of analyses yielded different decoding results on resting state data (Fig. 4: purple lines; Fig. 5: rightmost  
201 column). We note that, while the resting state times could be decoded reliably, the accuracies were only very  
202 slightly above chance. We speculate that the decoders might have picked up on attentional drift, boredom,  
203 or tiredness; we hypothesize that these all increased throughout the resting state scan. The decoders might  
204 be picking up on aspects of these loosely defined cognitive states that are common across individuals. The  
205 PCA-based approach achieved the highest resting state decoding accuracy using order zero features (non-  
206 correlational, activation-based), whereas the eigenvector centrality-based approach achieved the highest  
207 resting state decoding accuracy using second-order correlations. Taken together, these analyses indicate  
208 that high-level cognitive processing (while listening to the intact story) is reflected in the dynamics of high-  
209 order correlations in brain activity, whereas lower-level cognitive processing (while listening to scrambled  
210 versions of the story that lack rich meaning) is reflected in the dynamics of lower-order correlations and  
211 non-correlational activity dynamics. Further, these patterns are associated both with the underlying activity  
212 patterns (characterized using PCA) and also with the changing relative positions that different brain areas  
213 occupy in their associated networks (characterized using eigenvector centrality).

214 [Figure 6 about here.]

215 Having established that patterns of high-order correlations are informative to decoders, we next won-  
216 dered which specific networks of brain regions contributed most to these patterns. As a representative

example, we selected the kernel parameters that yielded decoding accuracies that were the most strongly correlated (across conditions and orders) with the average accuracies across all of the kernel parameters we examined. Using Figure 4c as a template, the best-matching kernel was a Laplace kernel with a width of 50 (Fig. 9d; also see Fig. S9). We used this kernel to compute a single  $K$  by  $K$   $n^{\text{th}}$ -order DISFC matrix for each experimental condition. We then used Neurosynth<sup>38</sup> to compute the terms most highly associated with the most strongly correlated pairs of regions in each of these matrices (Fig. 6; see Reverse inference).

For all of the story listening conditions (intact, paragraph, and word; top three rows of Fig. 6), we found that first- and second-order correlations were most strongly associated with auditory and speech processing areas. During intact story listening, third-order correlations reflected integration with visual areas, and fourth-order correlations reflected integration with areas associated with high-level cognition and cognitive control, such as the ventrolateral prefrontal cortex. However, when participants listened to temporally scrambled stories, these higher-order correlations instead involved interactions with additional regions associated with speech and semantic processing (second and third rows of Fig. 6). By contrast, we found a much different set of patterns in the resting state data (Fig. 6, bottom row). First-order resting state correlations were most strongly associated with regions involved in counting and numerical understanding. Second-order resting state correlations were strongest in visual areas; third-order correlations were strongest in task-positive areas; and fourth-order correlations were strongest in regions associated with autobiographical and episodic memory. We carried out analogous analyses to create maps (and decode the top associated Neurosynth terms) for up to fifteenth-order correlations (Figs. S5, S6, S7, and S8). Of note, examining fifteenth-order correlations between 700 nodes using conventional methods would have required storing roughly  $\frac{700^{2 \times 15}}{2} \approx 1.13 \times 10^{85}$  floating point numbers—assuming single-precision (32 bits each), this would require roughly 32 times as many bits as there are molecules in the known universe! Although these fifteenth-order correlations do appear (visually) to have some well-formed structure, we provide this latter example primarily as a demonstration of the efficiency and scalability of our approach.

## Discussion

We tested the hypothesis that high-level cognition is reflected in high-order brain network dynamics e.g., see<sup>19,26</sup>. We examined high-order network dynamics in functional neuroimaging data collected during a story listening experiment. When participants listened to an auditory recording of the story, participants exhibited similar high-order brain network dynamics. By contrast, when participants instead listened to temporally scrambled recordings of the story, only lower-order brain network dynamics were similar across participants. Our results indicate that higher orders of network interactions support higher-level aspects of

<sup>248</sup> cognitive processing (Fig. 7).

<sup>249</sup> [Figure 7 about here.]

<sup>250</sup> The notion that cognition is reflected in (and possibly mediated by) patterns of first-order network dy-  
<sup>251</sup> namics has been suggested by or proposed in myriad empirical studies and reviews e.g.,<sup>11,12,17,18,20–22,24,25,32,39–42</sup>.  
<sup>252</sup> Our study extends this line of work by finding cognitively relevant higher-order network dynamics that  
<sup>253</sup> reflect ongoing cognition. Our findings also complement other work that uses graph theory and topology  
<sup>254</sup> to characterize how brain networks reconfigure during cognition e.g.,<sup>16,26,30,31,34,35,43</sup>.

<sup>255</sup> An open question not addressed by our study pertains to how different structures integrate incoming  
<sup>256</sup> information with different time constants. For example, one line of work suggests that the cortical surface  
<sup>257</sup> comprises a structured map such that nearby brain structures process incoming information at similar  
<sup>258</sup> timescales. Low-level sensory areas integrate information relatively quickly, whereas higher-level regions  
<sup>259</sup> integrate information relatively slowly<sup>37,44–49</sup>. A similar hierarchy appears to play a role in predicting future  
<sup>260</sup> events<sup>50</sup>. Other related work in human and mouse brains indicates that the temporal response profile of a  
<sup>261</sup> given brain structure may relate to how strongly connected that structure is with other brain areas<sup>51</sup>. Further  
<sup>262</sup> study is needed to understand the role of temporal integration at different scales of network interaction,  
<sup>263</sup> and across different anatomical structures. Importantly, our analyses do not speak to the physiological  
<sup>264</sup> basis of higher-order dynamics, and could reflect nonlinearities, chaotic patterns, non-stationarities, and/or  
<sup>265</sup> multistability, etc. However, our decoding analyses do indicate that higher-order dynamics are consistent  
<sup>266</sup> across individuals, and therefore unlikely to reflect non-stimulus-driven dynamics that are unlikely to be  
<sup>267</sup> similar across individuals.

<sup>268</sup> Another potential limitation of our approach relates to recent work suggesting that the brain undergoes  
<sup>269</sup> rapid state changes, for example across event boundaries e.g.,<sup>44</sup><sup>52</sup> used hidden semi-Markov models to es-  
<sup>270</sup> timate state-specific network dynamics also see<sup>53</sup>. Our general approach might be extended by considering  
<sup>271</sup> putative state transitions. For example, rather than weighting all timepoints using a similar kernel (Eqn. 4),  
<sup>272</sup> the kernel function could adapt on a timepoint-by-timepoint basis such that only timepoints determined to  
<sup>273</sup> be in the same “state” were given non-zero weight.

<sup>274</sup> Identifying high-order network dynamics associated with high-level cognition required several impor-  
<sup>275</sup> tant methods advances. First, we used kernel-based dynamic correlations to extended the notion of (static)  
<sup>276</sup> inter-subject functional connectivity<sup>36</sup> to a dynamic measure of inter-subject functional connectivity (DISFC)  
<sup>277</sup> that does not rely on sliding windows e.g., as in<sup>11</sup>, and that may be computed at individual timepoints. This  
<sup>278</sup> allowed us to precisely characterize stimulus-evoked network dynamics that were similar across individ-  
<sup>279</sup> uals. Second, we developed a computational framework for efficiently and scalably estimating high-order

280 dynamic correlations. Our approach uses dimensionality reduction algorithms and graph measures to  
281 obtain low-dimensional embeddings of patterns of network dynamics. Third, we developed an analysis  
282 framework for identifying robust decoding results by carrying out our analyses using a range of parameter  
283 values and identifying which results were robust to specific parameter choices. By showing that high-level  
284 cognition is reflected in high-order network dynamics, we have elucidated the next step on the path towards  
285 understanding the neural basis of cognition.

## 286 Methods

287 Our general approach to efficiently estimating high-order dynamic correlations comprises four general  
288 steps (Fig. 8). First, we derive a kernel-based approach to computing dynamic pairwise correlations in  
289 a  $T$  (timepoints) by  $K$  (features) multivariate timeseries,  $\mathbf{X}_0$ . This yields a  $T$  by  $O(K^2)$  matrix of dynamic  
290 correlations,  $\mathbf{Y}_1$ , where each row comprises the upper triangle and diagonal of the correlation matrix at  
291 a single timepoint, reshaped into a row vector (this reshaped vector is  $(\frac{K^2-K}{2} + K)$ -dimensional). Second,  
292 we apply a dimensionality reduction step to project the matrix of dynamic correlations back onto a  $K$ -  
293 dimensional space. This yields a  $T$  by  $K$  matrix,  $\mathbf{X}_1$ , that reflects an approximation of the dynamic correlations  
294 reflected in the original data. Third, we use repeated applications of the kernel-based dynamic correlation  
295 step to  $\mathbf{X}_n$  and the dimensionality reduction step to the resulting  $\mathbf{Y}_{n+1}$  to estimate high-order dynamic  
296 correlations. Each application of these steps to a  $T$  by  $K$  time series  $\mathbf{X}_n$  yields a  $T$  by  $K$  matrix,  $\mathbf{X}_{n+1}$ , that  
297 reflects the dynamic correlations between the columns of  $\mathbf{X}_n$ . In this way, we refer to  $n$  as the order of the  
298 timeseries, where  $\mathbf{X}_0$  (order 0) denotes the original data and  $\mathbf{X}_n$  denotes (approximated)  $n^{\text{th}}$ -order dynamic  
299 correlations between the columns of  $\mathbf{X}_0$ . Finally, we use a cross-validation-based decoding approach to  
300 evaluate how well information contained in a given order (or weighted mixture of orders) may be used  
301 to decode relevant cognitive states. If including a given  $\mathbf{X}_n$  in the feature set yields higher classification  
302 accuracy on held-out data, we interpret this as evidence that the given cognitive states are reflected in  
303 patterns of  $n^{\text{th}}$ -order correlations.

304 All of the code used to produce the figures and results in this manuscript, along with links to the  
305 corresponding datasets, may be found at [github.com/ContextLab/timecorr-paper](https://github.com/ContextLab/timecorr-paper). In addition, we have  
306 released a Python toolbox for computing dynamic high-order correlations in timeseries data; our toolbox  
307 may be found at [timecorr.readthedocs.io](https://timecorr.readthedocs.io).

308

[Figure 8 about here.]

309 **Kernel-based approach for computing dynamic correlations**

Given a  $T$  by  $K$  matrix of observations,  $\mathbf{X}$ , we can compute the (static) Pearson's correlation between any pair of columns,  $\mathbf{X}(:, i)$  and  $\mathbf{X}(:, j)$  using<sup>29</sup>:

$$\text{corr}(\mathbf{X}(:, i), \mathbf{X}(:, j)) = \frac{\sum_{t=1}^T (\mathbf{X}(t, i) - \bar{\mathbf{X}}(:, i))(\mathbf{X}(t, j) - \bar{\mathbf{X}}(:, j))}{\sqrt{\sum_{t=1}^T \sigma_{\mathbf{X}(:, i)}^2 \sigma_{\mathbf{X}(:, j)}^2}}, \text{ where} \quad (1)$$

$$\bar{\mathbf{X}}(:, k) = \frac{1}{T} \sum_{t=1}^T \mathbf{X}(t, k), \text{ and} \quad (2)$$

$$\sigma_{\mathbf{X}(:, k)}^2 = \frac{1}{T} \sum_{t=1}^T (\mathbf{X}(t, k) - \bar{\mathbf{X}}(:, k))^2 \quad (3)$$

- 310 We can generalize this formula to compute time-varying correlations by incorporating a kernel function that  
 311 takes a time  $t$  as input, and returns how much the observed data at each timepoint  $\tau \in [-\infty, \infty]$  contributes  
 312 to the estimated instantaneous correlation at time  $t$  Fig. 9; also see<sup>54</sup> for a similar approach.

313 [Figure 9 about here.]

Given a kernel function  $\kappa_t(\cdot)$  for timepoint  $t$ , evaluated at timepoints  $\tau \in [1, \dots, T]$ , we can update the static correlation formula in Equation 1 to estimate the instantaneous correlation at timepoint  $t$ :

$$\text{timecorr}_{\kappa_t}(\mathbf{X}(:, i), \mathbf{X}(:, j)) = \frac{\sum_{\tau=1}^T (\mathbf{X}(\tau, i) - \tilde{\mathbf{X}}_{\kappa_t}(:, i))(\mathbf{X}(\tau, j) - \tilde{\mathbf{X}}_{\kappa_t}(:, j))}{\sqrt{\sum_{\tau=1}^T \tilde{\sigma}_{\kappa_t}^2(\mathbf{X}(:, i)) \tilde{\sigma}_{\kappa_t}^2(\mathbf{X}(:, j))}}, \text{ where} \quad (4)$$

$$\tilde{\mathbf{X}}_{\kappa_t}(:, k) = \sum_{\tau=1}^T \kappa_t(\tau) \mathbf{X}(\tau, k), \quad (5)$$

$$\tilde{\sigma}_{\kappa_t}^2(\mathbf{X}(:, k)) = \sum_{\tau=1}^T (\mathbf{X}(\tau, k) - \tilde{\mathbf{X}}_{\kappa_t}(:, k))^2. \quad (6)$$

- 314 Here  $\text{timecorr}_{\kappa_t}(\mathbf{X}(:, i), \mathbf{X}(:, j))$  reflects the correlation at time  $t$  between columns  $i$  and  $j$  of  $\mathbf{X}$ , estimated using  
 315 the kernel  $\kappa_t$ . We evaluate Equation 4 in turn for each pair of columns in  $\mathbf{X}$  and for kernels centered on each  
 316 timepoint in the timeseries, respectively, to obtain a  $T$  by  $K$  by  $K$  timeseries of dynamic correlations,  $\mathbf{Y}$ . For  
 317 convenience, we then reshape the upper triangles and diagonals of each timepoint's symmetric correlation  
 318 matrix into a row vector to obtain an equivalent  $T$  by  $(\frac{K^2-K}{2} + K)$  matrix.

319 **Dynamic inter-subject functional connectivity (DISFC)**

Equation 4 provides a means of taking a single observation matrix,  $\mathbf{X}_n$  and estimating the dynamic correlations from moment to moment,  $\mathbf{Y}_{n+1}$ . Suppose that one has access to a set of multiple observation

matrices that reflect the same phenomenon. For example, one might collect neuroimaging data from several experimental participants, as each participant performs the same task (or sequence of tasks). Let  $\mathbf{X}_n^1, \mathbf{X}_n^2, \dots, \mathbf{X}_n^P$  reflect the  $T$  by  $K$  observation matrices ( $n = 0$ ) or reduced correlation matrices ( $n > 0$ ) for each of  $P$  participants in an experiment. We can use inter-subject functional connectivity ISFC;<sup>36,55</sup> to compute the stimulus-driven correlations reflected in the multi-participant dataset at a given timepoint  $t$  using:

$$\bar{\mathbf{C}}(t) = M \left( R \left( \frac{1}{2P} \sum_{p=1}^P Z(\mathbf{Y}_{n+1}^p(t))^\top + Z(\mathbf{Y}_{n+1}^p(t)) \right) \right), \quad (7)$$

where  $M$  extracts and vectorizes the upper triangle and diagonal of a symmetric matrix,  $Z$  is the Fisher z-transformation<sup>56</sup>:

$$Z(r) = \frac{\log(1+r) - \log(1-r)}{2}, \quad (8)$$

$R$  is the inverse of  $Z$ :

$$R(z) = \frac{\exp(2z-1)}{\exp(2z+1)}, \quad (9)$$

and  $\mathbf{Y}_{n+1}^p(t)$  denotes the correlation matrix at timepoint  $t$  (Eqn. 4) between each column of  $\mathbf{X}_n^p$  and each column of the average  $\mathbf{X}_n$  from all other participants,  $\bar{\mathbf{X}}_n^{\setminus p}$ :

$$\bar{\mathbf{X}}_n^{\setminus p} = \frac{1}{P-1} \sum_{q \in \setminus p} \mathbf{X}_n^q, \quad (10)$$

320 where  $\setminus p$  denotes the set of all participants other than participant  $p$ . In this way, the  $T$  by  $(\frac{K^2-K}{2} + K)$  DISFC  
321 matrix  $\bar{\mathbf{C}}$  provides a time-varying extension of the ISFC approach developed by<sup>36</sup>.

### 322 Low-dimensional representations of dynamic correlations

323 Given a  $T$  by  $(\frac{K^2-K}{2} + K)$  matrix of  $n^{\text{th}}$ -order dynamic correlations,  $\mathbf{Y}_n$ , we propose two general approaches  
324 to computing a  $T$  by  $K$  low-dimensional representation of those correlations,  $\mathbf{X}_n$ . The first approach uses  
325 dimensionality reduction algorithms to project  $\mathbf{Y}_n$  onto a  $K$ -dimensional space. The second approach uses  
326 graph measures to characterize the relative positions of each feature ( $k \in [1, \dots, K]$ ) in the network defined  
327 by the correlation matrix at each timepoint.

328 **Dimensionality reduction-based approaches to computing  $\mathbf{X}_n$**

329 The modern toolkit of dimensionality reduction algorithms include Principal Components Analysis PCA;<sup>29</sup>,  
330 Probabilistic PCA PPCA;<sup>57</sup>, Exploratory Factor Analysis EFA;<sup>58</sup>, Independent Components Analysis ICA;<sup>59,60</sup>,  
331 *t*-Stochastic Neighbor Embedding *t*-SNE;<sup>61</sup>, Uniform Manifold Approximation and Projection UMAP;<sup>62</sup>,  
332 non-negative matrix factorization NMF;<sup>63</sup>, Topographic Factor Analysis TFA;<sup>64</sup>, Hierarchical Topographic  
333 Factor analysis HTFA;<sup>11</sup>, Topographic Latent Source Analysis TLSA;<sup>65</sup>, dictionary learning<sup>66,67</sup>, and deep  
334 auto-encoders<sup>68</sup>, among others. While complete characterizations of each of these algorithms is beyond the  
335 scope of the present manuscript, the general intuition driving these approaches is to compute the  $T$  by  $K$   
336 matrix,  $\mathbf{X}$ , that is closest to the original  $T$  by  $J$  matrix,  $\mathbf{Y}$ , where (typically)  $K \ll J$ . The different approaches  
337 place different constraints on what properties  $\mathbf{X}$  must satisfy and which aspects of the data are compared  
338 (and how) in order to optimize how well  $\mathbf{X}$  approximates  $\mathbf{Y}$ .

339 Applying dimensionality reduction algorithms to  $\mathbf{Y}$  yields an  $\mathbf{X}$  whose columns reflect weighted combi-  
340 nations (or nonlinear transformations) of the original columns of  $\mathbf{Y}$ . This has two main consequences. First,  
341 with each repeated dimensionality reduction, the resulting  $\mathbf{X}_n$  has lower and lower fidelity (with respect to  
342 what the “true”  $\mathbf{Y}_n$  might have looked like without using dimensionality reduction to maintain tractability).  
343 In other words, computing  $\mathbf{X}_n$  is a lossy operation. Second, whereas each column of  $\mathbf{Y}_n$  may be mapped  
344 directly onto specific pairs of columns of  $\mathbf{X}_{n-1}$ , the columns of  $\mathbf{X}_n$  reflect weighted combinations and/or  
345 nonlinear transformations of the columns of  $\mathbf{Y}_n$ . Many dimensionality reduction algorithms are invertible  
346 (or approximately invertible). However, attempting to map a given  $\mathbf{X}_n$  back onto the original feature space  
347 of  $\mathbf{X}_0$  will usually require  $O(TK^{2^n})$  space and therefore becomes intractable as  $n$  or  $K$  grow large.

348 **Graph measure approaches to computing  $\mathbf{X}_n$**

349 The above dimensionality reduction approaches to approximating a given  $\mathbf{Y}_n$  with a lower-dimensional  
350  $\mathbf{X}_n$  preserve a (potentially recombined and transformed) mapping back to the original data in  $\mathbf{X}_0$ . We also  
351 explore graph measures that instead characterize each feature’s relative position in the broader network of  
352 interactions and connections. To illustrate the distinction between the two general approaches we explore,  
353 suppose a network comprises nodes  $A$  and  $B$ , along with several other nodes. If  $A$  and  $B$  exhibit uncorrelated  
354 activity patterns, then by definition the functional connection (correlation) between them will be close to  
355 0. However, if  $A$  and  $B$  each interact with other nodes in similar ways, we might attempt to capture those  
356 similarities between  $A$ ’s and  $B$ ’s interactions with those other members of the network.

357 In general, graph measures take as input a matrix of interactions (e.g., using the above notation, a  $K$   
358 by  $K$  correlation matrix or binarized correlation matrix reconstituted from a single timepoint’s row of  $\mathbf{Y}$ ),

359 and return as output a set of  $K$  measures describing how each node (feature) sits within that correlation  
360 matrix with respect to the rest of the population. Widely used measures include betweenness centrality the  
361 proportion of shortest paths between each pair of nodes in the population that involves the given node in  
362 question; e.g.,<sup>69–73</sup>; diversity and dissimilarity characterizations of how differently connected a given node  
363 is from others in the population; e.g.,<sup>74–76</sup>; eigenvector centrality and pagerank centrality measures of how  
364 influential a given node is within the broader network; e.g.,<sup>77–80</sup>; transfer entropy and flow coefficients a  
365 measure of how much information is flowing from a given node to other nodes in the network; e.g.,<sup>81,82</sup>;  
366  $k$ -coreness centrality a measure of the connectivity of a node within its local subgraph; e.g.,<sup>83,84</sup>; within-  
367 module degree a measure of how many connections a node has to its close neighbors in the network;  
368 e.g.,<sup>85</sup>; participation coefficient a measure of the diversity of a node's connections to different subgraphs  
369 in the network; e.g.,<sup>85</sup>; and subgraph centrality a measure of a node's participation in all of the network's  
370 subgraphs; e.g.,<sup>86</sup>; among others.

371 For a given graph measure,  $\eta : \mathbb{R}^{K \times K} \rightarrow \mathbb{R}^K$ , we can use  $\eta$  to transform each row of  $\mathbf{Y}_n$  in a way that  
372 characterizes the corresponding graph properties of each column. This results in a new  $T$  by  $K$  matrix,  
373  $\mathbf{X}_n$ , that reflects how the features reflected in the columns of  $\mathbf{X}_{n-1}$  participate in the network during each  
374 timepoint (row).

### 375 **Dynamic higher-order correlations**

376 Because  $\mathbf{X}_n$  has the same shape as the original data  $\mathbf{X}_0$ , approximating  $\mathbf{Y}_n$  with a lower-dimensional  $\mathbf{X}_n$   
377 enables us to estimate high-order dynamic correlations in a scalable way. Given a  $T$  by  $K$  input matrix, the  
378 output of Equation 4 requires  $O(TK^2)$  space to store. Repeated applications of Equation 4 (i.e., computing  
379 dynamic correlations between the columns of the outputted dynamic correlation matrix) each require  
380 exponentially more space; in general the  $n^{\text{th}}$ -order dynamic correlations of a  $T$  by  $K$  timeseries occupies  
381  $O(TK^{2^n})$  space. However, when we approximate or summarize the output of Equation 4 with a  $T$  by  $K$  matrix  
382 (as described above), it becomes feasible to compute even very high-order correlations in high-dimensional  
383 data. Specifically, approximating the  $n^{\text{th}}$ -order dynamic correlations of a  $T$  by  $K$  timeseries requires only  
384  $O(TK^2)$  additional space— the same as would be required to compute first-order dynamic correlations. In  
385 other words, the space required to store  $n + 1$  multivariate timeseries reflecting up to  $n^{\text{th}}$  order correlations  
386 in the original data scales linearly with  $n$  using our approach (Fig. 8).

387 **Data**

388 We examined two types of data: synthetic data and human functional neuroimaging data. We constructed  
389 and leveraged the synthetic data to evaluate our general approach for a related validation approach see<sup>87</sup>.  
390 Specifically, we tested how well Equation 4 could be used to recover known dynamic correlations using  
391 different choices of kernel ( $\kappa$ ; Fig. 9), for each of several synthetic datasets that exhibited different temporal  
392 properties. We also simulated higher-order correlations and tested how well Equation 4 could recover these  
393 correlations using the best kernel from the previous synthetic data analyses. We then applied our approach  
394 to a functional neuroimaging dataset to test the hypothesis that ongoing cognitive processing is reflected  
395 in high-order dynamic correlations. We used an across-participant classification test to estimate whether  
396 dynamic correlations of different orders contain information about which timepoint in a story participants  
397 were listening to.

398 **Synthetic data: simulating dynamic first-order correlations**

399 We constructed a total of 400 different multivariate timeseries, collectively reflecting a total of 4 qualitatively  
400 different patterns of dynamic first-order correlations (i.e., 100 datasets reflecting each type of dynamic pat-  
401 tern). Each timeseries comprised 50 features (dimensions) that varied over 300 timepoints. The observations  
402 at each timepoint were drawn from a zero-mean multivariate Gaussian distribution with a covariance matrix  
403 defined for each timepoint as described below. We drew the observations at each timepoint independently  
404 from the draws at all other timepoints; in other words, for each observation  $s_t \sim \mathcal{N}(\mathbf{0}, \Sigma_t)$  at timepoint  $t$ ,  
405  $p(s_t) = p(s_t | s_{\setminus t})$ .

**Constant.** We generated data with stable underlying correlations to evaluate how Equation 4 characterized correlation “dynamics” when the ground truth correlations were static. We constructed 100 multivariate timeseries whose observations were each drawn from a single (stable) Gaussian distribution. For each dataset (indexed by  $m$ ), we constructed a random covariance matrix,  $\Sigma_m$ :

$$\Sigma_m = \mathbf{C}\mathbf{C}^\top, \text{ where} \quad (11)$$

$$\mathbf{C}(i, j) \sim \mathcal{N}(0, 1), \text{ and where} \quad (12)$$

406  $i, j \in [1, 2, \dots, 50]$ . In other words, all of the observations (for each of the 300 timepoints) within each dataset  
407 were drawn from a multivariate Gaussian distribution with the same covariance matrix, and the 100 datasets  
408 each used a different covariance matrix.

409 **Random.** We generated a second set of 100 synthetic datasets whose observations at each timepoint were  
 410 drawn from a Gaussian distribution with a new randomly constructed (using Eqn. 11) covariance matrix.  
 411 Because each timepoint’s covariance matrix was drawn independently from the covariance matrices for all  
 412 other timepoints, these datasets provided a test of reconstruction accuracy in the absence of any meaningful  
 413 underlying temporal structure in the dynamic correlations underlying the data.

**Ramping.** We generated a third set of 100 synthetic datasets whose underlying correlations changed gradually over time. For each dataset, we constructed two anchor covariance matrices using Equation 11,  $\Sigma_{\text{start}}$  and  $\Sigma_{\text{end}}$ . For each of the 300 timepoints in each dataset, we drew the observations from a multivariate Gaussian distribution whose covariance matrix at each timepoint  $t \in [0, \dots, 299]$  was given by

$$\Sigma_t = \left(1 - \frac{t}{299}\right)\Sigma_{\text{start}} + \frac{t}{299}\Sigma_{\text{end}}. \quad (13)$$

414 The gradually changing correlations underlying these datasets allow us to evaluate the recovery of dynamic  
 415 correlations when each timepoint’s correlation matrix is unique (as in the random datasets), but where the  
 416 correlation dynamics are structured and exhibit first-order autocorrelations (as in the constant datasets).

417 **Event.** We generated a fourth set of 100 synthetic datasets whose underlying correlation matrices exhibited  
 418 prolonged intervals of stability, interspersed with abrupt changes. For each dataset, we used Equation 11  
 419 to generate 5 random covariance matrices. We constructed a timeseries where each set of 60 consecutive  
 420 samples was drawn from a Gaussian with the same covariance matrix. These datasets were intended to  
 421 simulate a system that exhibits periods of stability punctuated by occasional abrupt state changes.

## 422 Synthetic data: simulating dynamic high-order correlations

423 We developed an iterative procedure for constructing timeseries data that exhibits known dynamic high-  
 424 order correlations. The procedure builds on our approach to generating dynamic first-order correlations.  
 425 Essentially, once we generate a timeseries with known first-order correlations, we can use the known first-  
 426 order correlations as a template to generate a new timeseries of second-order correlations. In turn, we can  
 427 generate a timeseries of third-order correlations from the second-order correlations, and so on. In general,  
 428 we can generate order  $n$  correlations given a timeseries of order  $n - 1$  correlations, for any  $n > 1$ . Finally,  
 429 given the order  $n$  timeseries, we can reverse the preceding process to generate an order  $n - 1$  timeseries, an  
 430 order  $n - 2$  order timeseries, and so on, until we obtain an order 0 timeseries of simulated data that reflects  
 431 the chosen high-order dynamics.

432 The central mathematical operation in our procedure is the Kronecker product ( $\otimes$ ). The Kronecker  
433 product of a  $K \times K$  matrix,  $m_1$ , with itself (i.e.,  $m_1 \otimes m_1$ ) produces a new  $K^2 \times K^2$  matrix,  $m_2$  whose entries  
434 reflect a scaled tiling of the entries in  $m_1$ . If these tilings (scaled copies of  $m_1$ ) are indexed by row and column,  
435 then the tile in the  $i^{\text{th}}$  row and  $j^{\text{th}}$  column contains the entries of  $m_1$ , multiplied by  $m_1(i, j)$ . Following this  
436 pattern, the Kronecker product  $m_2 \otimes m_2$  yields the  $K^4 \times K^4$  matrix  $m_3$  whose tiles are scaled copies of  $m_2$ . In  
437 general, repeated applications of the Kronecker self-product may be used to generate  $m_{n+1} = m_n \otimes m_n$  for  
438  $n > 1$ , where  $m_{n+1}$  is a  $K^{2^n} \times K^{2^n}$  matrix. After generating a first-order timeseries of dynamic correlations (see  
439 Synthetic data: simulating dynamic first-order correlations), we use this procedure (applied independently  
440 at each timepoint) to transform it into a timeseries of  $n^{\text{th}}$ -order correlations. When  $m_{n+1}$  is generated in this  
441 way, the temporal structure of the full timeseries (i.e., constant, random, ramping, event) is preserved, since  
442 changes in the original first-order timeseries are also reflected in the scaled tilings of itself that comprise the  
443 higher-order matrices.

444 Given a timeseries of  $n^{\text{th}}$ -order correlations, we then need to work “backwards” in order to generate the  
445 order-zero timeseries. If the  $n^{\text{th}}$ -order correlation matrix at a given timepoint is  $m_n$ , then we can generate an  
446 order  $n - 1$  correlation matrix (for  $n > 1$ ) by taking a draw from  $\mathcal{N}(0, m_n)$  and reshaping the resulting vector  
447 to have square dimensions. Intuitively, the re-shaped matrix will look like a noisy version of the template  
448 matrix,  $m_{n-1}$ . (When  $n = 1$ , no re-shaping is needed; the resulting  $K$ -dimensional vector may be used as the  
449 observation at the given timepoint.) After independently drawing each timepoint’s order  $n - 1$  correlation  
450 matrix from that timepoint’s order  $n$  correlation matrix, this process can be applied repeatedly until  $n = 0$ .  
451 This results in a  $K$ -dimensional timeseries of  $T$  observations containing the specified high-order correlations  
452 at orders 1 through  $n$ . Following our approach to generating synthetic data exhibiting known first-order  
453 correlations, we constructed a total of 400 additional multivariate timeseries, collectively reflecting a total of  
454 4 qualitatively different patterns of dynamic correlations (i.e., 100 datasets reflecting each type of dynamic  
455 pattern: constant, random, ramping, and event). Each timeseries comprised 10 features (dimensions) that  
456 varied over 300 timepoints for first-order correlations, and therefore 100 second-order features.

457 **Functional neuroimaging data collected during story listening**

458 We examined an fMRI dataset collected by<sup>36</sup> that the authors have made publicly available at [arks.princeton.edu/ark:/88435/ds](https://arks.princeton.edu/ark:/88435/ds).  
459 The dataset comprises neuroimaging data collected as participants listened to an audio recording of a story  
460 (intact condition; 36 participants), listened to temporally scrambled recordings of the same story (17 partici-  
461 pants in the paragraph-scrambled condition listened to the paragraphs in a randomized order and 36 in the  
462 word-scrambled condition listened to the words in a randomized order), or lay resting with their eyes open

463 in the scanner (rest condition; 36 participants). Full neuroimaging details may be found in the original paper  
464 for which the data were collected<sup>36</sup>. Procedures were approved by the Princeton University Committee  
465 on Activities Involving Human Subjects, and by Western Institutional Review Board (Puyallup, WA). All  
466 subjects were native English speakers with normal hearing and provided written informed consent.

467 **Hierarchical topographic factor analysis (HTFA).** Following our prior related work, we used HTFA<sup>11</sup>  
468 to derive a compact representation of the neuroimaging data. In brief, this approach approximates the  
469 timeseries of voxel activations (44,415 voxels) using a much smaller number of radial basis function (RBF)  
470 nodes in this case, 700 nodes, as determined by an optimization procedure described by<sup>11</sup>. This provides  
471 a convenient representation for examining full-brain network dynamics. All of the analyses we carried  
472 out on the neuroimaging dataset were performed in this lower-dimensional space. In other words, each  
473 participant's data matrix,  $\mathbf{X}_0$ , was a number-of-timepoints by 700 matrix of HTFA-derived factor weights  
474 (where the row and column labels were matched across participants). Code for carrying out HTFA on fMRI  
475 data may be found as part of the BrainIAK toolbox<sup>88</sup>, which may be downloaded at [brainiak.org](http://brainiak.org).

## 476 **Temporal decoding**

477 We sought to identify neural patterns that reflected participants' ongoing cognitive processing of incoming  
478 stimulus information. As reviewed by<sup>36</sup>, one way of homing in on these stimulus-driven neural patterns  
479 is to compare activity patterns across individuals (e.g., using ISFC analyses). In particular, neural patterns  
480 will be similar across individuals to the extent that the neural patterns under consideration are stimulus-  
481 driven, and to the extent that the corresponding cognitive representations are reflected in similar spatial  
482 patterns across people also see<sup>55</sup>. Following this logic, we used an across-participant temporal decoding test  
483 developed by<sup>11</sup> to assess the degree to which different neural patterns reflected ongoing stimulus-driven  
484 cognitive processing across people (Fig. 10). The approach entails using a subset of the data to train a  
485 classifier to decode stimulus timepoints (i.e., moments in the story participants listened to) from neural  
486 patterns. We use decoding (forward inference) accuracy on held-out data, from held-out participants, as a  
487 proxy for the extent to which the inputted neural patterns reflected stimulus-driven cognitive processing in  
488 a similar way across individuals.

## 489 **Forward inference and decoding accuracy**

490 We used an across-participant correlation-based classifier to decode which stimulus timepoint matched  
491 each timepoint's neural pattern(Fig. 10. We first divided the participants into two groups: a template group,

492  $\mathcal{G}_{\text{template}}$  (i.e., training data), and a to-be-decoded group,  $\mathcal{G}_{\text{decode}}$  (i.e., test data). We used Equation 7 to  
493 compute a DISFC matrix for each group ( $\bar{\mathbf{C}}_{\text{template}}$  and  $\bar{\mathbf{C}}_{\text{decode}}$ , respectively). We then correlated the rows of  
494  $\bar{\mathbf{C}}_{\text{template}}$  and  $\bar{\mathbf{C}}_{\text{decode}}$  to form a number-of-timepoints by number-of-timepoints decoding matrix,  $\Lambda$ . In this  
495 way, the rows of  $\Lambda$  reflected timepoints from the template group, while the columns reflected timepoints  
496 from the to-be-decoded group. We used  $\Lambda$  to assign temporal labels to each row  $\bar{\mathbf{C}}_{\text{decode}}$  using the row of  
497  $\bar{\mathbf{C}}_{\text{template}}$  with which it was most highly correlated. We then repeated this decoding procedure, but using  
498  $\mathcal{G}_{\text{decode}}$  as the template group and  $\mathcal{G}_{\text{template}}$  as the to-be-decoded group. Given the true timepoint labels (for  
499 each group), we defined the decoding accuracy as the average proportion of correctly decoded timepoints,  
500 across both groups. We defined the relative decoding accuracy as the difference between the decoding  
501 accuracy and chance accuracy (i.e.,  $\frac{1}{T}$ ).

502 **Feature weighting and testing**

503 We sought to examine which types of neural features (i.e., activations, first-order dynamic correlations, and  
504 higher-order dynamic correlations) were informative to the temporal decoders. Using the notation above,  
505 these features correspond to  $\mathbf{X}_0, \mathbf{X}_1, \mathbf{X}_2, \mathbf{X}_3$ , and so on.

506 [Figure 10 about here.]

507 One challenge to fairly evaluating high-order correlations is that if the kernel used in Equation 4 is  
508 wider than a single timepoint, each repeated application of the equation will result in further temporal  
509 blur. Because our primary assessment metric is temporal decoding accuracy, this unfairly biases against  
510 detecting meaningful signal in higher-order correlations (relative to lower-order correlations). We attempted  
511 to mitigate temporal blur in estimating each  $\mathbf{X}_n$  by using a Dirac  $\delta$  function kernel (which places all of its  
512 mass over a single timepoint; Fig. 9b, 10a) to compute each lower-order correlation ( $\mathbf{X}_1, \mathbf{X}_2, \dots, \mathbf{X}_{n-1}$ ). We  
513 then used a new (potentially wider, as described below) kernel to compute  $\mathbf{X}_n$  from  $\mathbf{X}_{n-1}$ . In this way,  
514 temporal blurring was applied only in the last step of computing  $\mathbf{X}_n$ . We note that, because each  $\mathbf{X}_n$  is a  
515 low-dimensional representation of the corresponding  $\mathbf{Y}_n$ , the higher-order correlations we estimated reflect  
516 true correlations in the data with lower-fidelity than estimates of lower-order correlations. Therefore, even  
517 after correcting for temporal blurring, our approach is still biased against finding meaningful signal in  
518 higher-order correlations.

519 After computing each  $\mathbf{X}_1, \mathbf{X}_2, \dots, \mathbf{X}_{n-1}$  for each participant, we divided participants into two equally sized  
520 groups ( $\pm 1$  for odd numbers of participants):  $\mathcal{G}_{\text{train}}$  and  $\mathcal{G}_{\text{test}}$ . We then further subdivided  $\mathcal{G}_{\text{train}}$  into  $\mathcal{G}_{\text{train}_1}$   
521 and  $\mathcal{G}_{\text{train}_2}$ . We then computed  $\Lambda$  (temporal correlation) matrices for each type of neural feature, using  $\mathcal{G}_{\text{train}_1}$   
522 and  $\mathcal{G}_{\text{train}_2}$ . This resulted in  $n + 1$   $\Lambda$  matrices (one for the original timeseries of neural activations, and one

523 for each of  $n$  orders of dynamic correlations). Our objective was to find a set of weights for each of these  
524  $\Lambda$  matrices such that the weighted average of the  $n + 1$  matrices yielded the highest decoding accuracy.  
525 We used quasi-Newton gradient ascent<sup>89</sup>, using decoding accuracy (for  $\mathcal{G}_{\text{train}_1}$  and  $\mathcal{G}_{\text{train}_2}$ ) as the objective  
526 function to be maximized, to find an optimal set of training data-derived weights,  $\phi_{0,1,\dots,n}$ , where  $\sum_{i=0}^n \phi_i = 1$   
527 and where  $\phi_i \geq 0 \forall i \in [0, 1, \dots, n]$ .

528 After estimating an optimal set of weights, we computed a new set of  $n + 1$   $\Lambda$  matrices correlating the  
529 DISFC patterns from  $\mathcal{G}_{\text{train}}$  and  $\mathcal{G}_{\text{test}}$  at each timepoint. We use the resulting decoding accuracy of  $\mathcal{G}_{\text{test}}$   
530 timepoints (using the weights in  $\phi_{0,1,\dots,n}$  to average the  $\Lambda$  matrices) to estimate how informative the set of  
531 neural features containing up to  $n^{\text{th}}$  order correlations were.

532 We used a permutation-based procedure to form stable estimates of decoding accuracy for each set of  
533 neural features. In particular, we computed the decoding accuracy for each of 10 random group assignments  
534 of  $\mathcal{G}_{\text{train}}$  and  $\mathcal{G}_{\text{test}}$ . We report the mean accuracy (along with 95% confidence intervals) for each set of neural  
535 features.

### 536 Identifying robust decoding results

537 The temporal decoding procedure we use to estimate which neural features support ongoing cognitive  
538 processing is governed by several parameters. In particular, Equation 4 requires defining a kernel function,  
539 which can take on different shapes and widths. For a fixed set of neural features, each of these parameters  
540 can yield different decoding accuracies. Further, the best decoding accuracy for a given timepoint may be  
541 reliably achieved by one set of parameters, whereas the best decoding accuracy for another timepoint might  
542 be reliably achieved by a different set of parameters, and the best decoding accuracy across all timepoints  
543 might be reliably achieved by still another different set of parameters. Rather than attempting to maximize  
544 decoding accuracy, we sought to discover the trends in the data that were robust to classifier parameters  
545 choices. Specifically, we sought to characterize how decoding accuracy varied (under different experimental  
546 conditions) as a function of which neural features were considered.

547 To identify decoding results that were robust to specific classifier parameter choices, we repeated our  
548 decoding analyses after substituting into Equation 4 each of a variety of kernel shapes and widths. We  
549 examined Gaussian (Fig. 9c), Laplace (Fig. 9d), and Mexican Hat (Fig. 9e) kernels, each with widths of 5, 10,  
550 20, and 50 samples. We then report the average decoding accuracies across all of these parameter choices.  
551 This enabled us to (partially) factor out performance characteristics that were parameter-dependent, within  
552 the set of parameters we examined.

553 **Reverse inference**

554 The dynamic patterns we examined comprise high-dimensional correlation patterns at each timepoint. To  
555 help interpret the resulting patterns in the context of other studies, we created summary maps by computing  
556 the across-timepoint average pairwise correlations at each order of analysis (first order, second order, etc.).  
557 We selected the 10 strongest (absolute value) correlations at each order. Each correlation is between the  
558 dynamic activity patterns (or patterns of dynamic high-order correlations) measured at two RBF nodes (see  
559 Hierarchical Topographic Factor Analysis). Therefore, the 10 strongest correlations involved up to 20 RBF  
560 nodes. Each RBF defines a spatial function whose activations range from 0 to 1. We constructed a map  
561 of RBF components that denoted the endpoints of the 10 strongest correlations (we set each RBF to have a  
562 maximum value of 1). We then carried out a meta analysis using Neurosynth<sup>38</sup> to identify the 10 terms most  
563 commonly associated with the given map. This resulted in a set of 10 terms associated with the average  
564 dynamic correlation patterns at each order.

565 **Data Availability**

566 The authors declare that the data supporting the findings of this study as well as the source data for this  
567 paper are available at [github.com/ContextLab/timecorr-paper/releases/tag/v0.3](https://github.com/ContextLab/timecorr-paper/releases/tag/v0.3). The fMRI dataset collected  
568 by<sup>36</sup> has been made publicly available at [arks.princeton.edu/ark:/88435/dsp015d86p269k](https://arks.princeton.edu/ark:/88435/dsp015d86p269k)

569 **Acknowledgements**

570 We acknowledge discussions with Luke Chang, Vassiki Chauhan, Hany Farid, Paxton Fitzpatrick, Andrew  
571 Heusser, Eshin Jolly, Aaron Lee, Qiang Liu, Matthijs van der Meer, Judith Mildner, Gina Notaro, Stephen  
572 Satterthwaite, Emily Whitaker, Weizhen Xie, and Kirsten Ziman. Our work was supported in part by NSF  
573 EPSCoR Award Number 1632738 to J.R.M. and by a sub-award of DARPA RAM Cooperative Agreement  
574 N66001-14-2-4-032 to J.R.M. The content is solely the responsibility of the authors and does not necessarily  
575 represent the official views of our supporting organizations.

576 **Author contributions**

577 Concept: J.R.M. Implementation: T.H.C., L.L.W.O., and J.R.M. Analyses: L.L.W.O. and J.R.M. Writing:  
578 L.L.W.O. and J.R.M.

579 **Competing interests**

580 The authors declare no competing financial interests.

581 **References**

- 582 [1] Haxby, J. V. *et al.* Distributed and overlapping representations of faces and objects in ventral temporal  
583 cortex. *Science* **293**, 2425–2430 (2001).
- 584 [2] Norman, K. A., Polyn, S. M., Detre, G. J. & Haxby, J. V. Beyond mind-reading: multi-voxel pattern  
585 analysis of fMRI data. *Trends in Cognitive Sciences* **10**, 424–430 (2006).
- 586 [3] Tong, F. & Pratte, M. S. Decoding patterns of human brain activity. *Annual Review of Psychology* **63**,  
587 483–509 (2012).
- 588 [4] Mitchell, T. M. *et al.* Predicting human brain activity associated with the meanings of nouns. *Science*  
589 **320**, 1191 (2008).
- 590 [5] Kamitani, Y. & Tong, F. Decoding the visual and subjective contents of the human brain. *Nature  
591 Neuroscience* **8**, 679–685 (2005).
- 592 [6] Nishimoto, S. *et al.* Reconstructing visual experience from brain activity evoked by natural movies.  
593 *Current Biology* **21**, 1–6 (2011).
- 594 [7] Pereira, F. *et al.* Toward a universal decoder of linguistic meaning from brain activation. *Nature  
595 Communications* **9**, 1–13 (2018).
- 596 [8] Huth, A. G., Nisimoto, S., Vu, A. T. & Gallant, J. L. A continuous semantic space describes the  
597 representation of thousands of object and action categories across the human brain. *Neuron* **76**, 1210–  
598 1224 (2012).
- 599 [9] Huth, A. G., de Heer, W. A., Griffiths, T. L., Theunissen, F. E. & Gallant, J. L. Natural speech reveals the  
600 semantic maps that tile human cerebral cortex. *Nature* **532**, 453–458 (2016).
- 601 [10] Etzel, J. A., Gazzola, V. & Keysers, C. An introduction to anatomical ROI-based fMRI classification.  
602 *Brain Research* **1281**, 114–125 (2009).
- 603 [11] Manning, J. R. *et al.* A probabilistic approach to discovering dynamic full-brain functional connectivity  
604 patterns. *NeuroImage* **180**, 243–252 (2018).

- 605 [12] Fong, A. H. C. *et al.* Dynamic functional connectivity during task performance and rest predicts  
606 individual differences in attention across studies. *NeuroImage* **188**, 14–25 (2019).
- 607 [13] Grossberg, S. Nonlinear neural networks: principles, mechanisms, and architectures. *Neural Networks*  
608 **1**, 17–61 (1988).
- 609 [14] Friston, K. J. The labile brain. I. neuronal transients and nonlinear coupling. *Philosophical Transactions  
610 of the Royal Society of London* **355B**, 215–236 (2000).
- 611 [15] Sporns, O. & Honey, C. J. Small worlds inside big brains. *Proceedings of the National Academy of Sciences,  
612 USA* **103**, 19219–19220 (2006).
- 613 [16] Bassett, D., Meyer-Lindenberg, A., Achard, S., Duke, T. & Bullmore, E. Adaptive reconfiguration of  
614 fractal small-world human brain functional networks. *Proceedings of the National Academy of Sciences,  
615 USA* **103**, 19518–19523 (2006).
- 616 [17] Turk-Browne, N. B. Functional interactions as big data in the human brain. *Science* **342**, 580–584 (2013).
- 617 [18] Demertzi, A. *et al.* Human consciousness is supported by dynamic complex patterns of brain signal  
618 coordination. *Science Advances* **5**, eaat7603 (2019).
- 619 [19] Solomon, S. H., Medaglia, J. D. & Thompson-Schill, S. L. Implementing a concept network model.  
620 *Behavior Research Methods* **51**, 1717–1736 (2019).
- 621 [20] Lurie, D. *et al.* On the nature of time-varying functional connectivity in resting fMRI. *PsyArXiv  
622 doi.org/10.31234/osf.io/xtzre* (2018).
- 623 [21] Preti, M. G., Bolton, T. A. W. & Van De Ville, D. The dynamic functional connectome: state-of-the-art  
624 and perspectives. *NeuroImage* **160**, 41–54 (2017).
- 625 [22] Zou, Y., Donner, R. V., Marwan, N., Donges, J. F. & Kurths, J. Complex network approaches to nonlinear  
626 time series analysis. *Physics Reports* **787**, 1–97 (2019).
- 627 [23] Mack, M. L., Preston, A. R. & Love, B. C. Medial prefrontal cortex compresses concept representations  
628 through learning. *bioRxiv doi.org/10.1101/178145* (2017).
- 629 [24] Bressler, S. L. & Kelso, J. A. S. Cortical coordination dynamics and cognition. *Trends in Cognitive Sciences*  
630 **5**, 26–36 (2001).
- 631 [25] McIntosh, A. R. Towards a network theory of cognition. *Neural Networks* **13**, 861–870 (2000).

- 632 [26] Reimann, M. W. *et al.* Cliques of neurons bound into cavities provide a missing link between structure  
633 and function. *Frontiers in Computational Neuroscience* **11**, 1–16 (2017).
- 634 [27] Beaty, R. E., Benedek, M., Silvia, P. J. & Schacter, D. L. Creative cognition and brain network dynamics.  
635 *Trends in Cognitive Sciences* **20**, 87–95 (2016).
- 636 [28] Bullmore, E. & Sporns, O. Complex brain networks: graph theoretical analysis of structural and  
637 functional systems. *Nature Reviews Neuroscience* **10**, 186–198 (2009).
- 638 [29] Pearson, K. On lines and planes of closest fit to systems of points in space. *The London, Edinburgh, and*  
639 *Dublin Philosophical Magazine and Journal of Science* **2**, 559–572 (1901).
- 640 [30] McIntosh, A. R. & Jirsa, V. K. The hidden repertoire of brain dynamics and dysfunction. *Network*  
641 *Neuroscience* [doi.org/10.1162/netn\\_a.00107](https://doi.org/10.1162/netn_a.00107) (2019).
- 642 [31] Toker, D. & Sommer, F. T. Information integration in large brain networks. *PLoS Computational Biology*  
643 **15**, e1006807 (2019).
- 644 [32] Gonzalez-Castillo, J. *et al.* Imaging the spontaneous flow of thought: distinct periods of cognition  
645 contribute to dynamic functional connectivity during rest. *NeuroImage* **202** (2019).
- 646 [33] Landau, E. Zur relativen Wertbemessung der Turnierresultate. *Deutsches Wochenschach* **11**, 366–369  
647 (1895).
- 648 [34] Betzel, R. F., Byrge, L., Esfahlani, F. Z. & Kennedy, D. P. Temporal fluctuations in the brain's modular  
649 architecture during movie-watching. *bioRxiv* [doi.org/10.1101/750919](https://doi.org/10.1101/750919) (2019).
- 650 [35] Sizemore, A. E. *et al.* Cliques and cavities in the human connectome. *Journal of Computational Neuroscience*  
651 **44**, 115–145 (2018).
- 652 [36] Simony, E., Honey, C. J., Chen, J. & Hasson, U. Dynamic reconfiguration of the default mode network  
653 during narrative comprehension. *Nature Communications* **7**, 1–13 (2016).
- 654 [37] Hasson, U., Yang, E., Vallines, I., Heeger, D. J. & Rubin, N. A hierarchy of temporal receptive windows  
655 in human cortex. *The Journal of Neuroscience* **28**, 2539–2550 (2008).
- 656 [38] Rubin, T. N. *et al.* Decoding brain activity using a large-scale probabilistic functional-anatomical atlas  
657 of human cognition. *PLoS Computational Biology* **13**, e1005649 (2017).
- 658 [39] Park, H.-J., Friston, K. J., Pae, C., Park, B. & Razi, A. Dynamic effective connectivity in resting state  
659 fMRI. *NeuroImage* **180**, 594–608 (2018).

- 660 [40] Roy, D. S. *et al.* Brain-wide mapping of contextual fear memory ensembles supports the  
661 dispersed engram complex hypothesis. *bioRxiv* doi.org/10.1101/668483 (2019).
- 662 [41] Liégeois, R. *et al.* Resting brain dynamics at different timescales capture distinct aspects of human  
663 behavior. *Nature Communications* **10**, 1–9 (2019).
- 664 [42] Chang, C. & Glover, G. H. Time-frequency dynamics of resting-state brain connectivity measured with  
665 fMRI. *NeuroImage* **50**, 81–98 (2010).
- 666 [43] Zheng, M., Allard, A., Hagmann, P. & Serrano, M. . . A. Geometric renormalization unravels self-  
667 similarity of the multiscale human connectome. *arXiv* 1904.11793 (2019).
- 668 [44] Baldassano, C. *et al.* Discovering event structure in continuous narrative perception and memory.  
669 *Neuron* **95**, 709–721 (2017).
- 670 [45] Hasson, U., Chen, J. & Honey, C. J. Hierarchical process memory: memory as an integral component  
671 of information processing. *Trends in Cognitive Sciences* **19**, 304–315 (2015).
- 672 [46] Honey, C. J. *et al.* Slow cortical dynamics and the accumulation of information over long timescales.  
673 *Neuron* **76**, 423–434 (2012).
- 674 [47] Lerner, Y., Honey, C. J., Silbert, L. J. & Hasson, U. Topographic mapping of a hierarchy of temporal  
675 receptive windows using a narrated story. *The Journal of Neuroscience* **31**, 2906–2915 (2011).
- 676 [48] Lerner, Y., Honey, C. J., Katkov, M. & Hasson, U. Temporal scaling of neural responses to compressed  
677 and dilated natural speech. *Journal of Neurophysiology* **111**, 2433–2444 (2014).
- 678 [49] Chien, H.-Y. S. & Honey, C. J. Constructing and forgetting temporal context in the human cerebral  
679 cortex. *bioRxiv* doi.org/10.1101/761593 (2019).
- 680 [50] Lee, C. S., Aly, M. & Baldassano, C. Anticipation of temporally structured events in the brain. *bioRxiv*  
681 10.1101/2020.10.14.338145 (2020).
- 682 [51] Fallon, J., Ward, P. G. D., Parkes, L. & Oldham, S. Timescales of spontaneous fMRI fluctuations relate  
683 to structural connectivity in the brain. *Network Neuroscience* **4**, 788–806 (2020).
- 684 [52] Shappell, H., Caffo, B. S., Pekar, J. J. & Lindquist, M. A. Improved state change estimation in dynamic  
685 functional connectivity using hidden semi-Markov models. *NeuroImage* **191**, 243–257 (2019).
- 686 [53] Vidaurre, D. *et al.* Discovering dynamic brain networks from big data in rest and task. *NeuroImage* **180**,  
687 646–656 (2018).

- 688 [54] Allen, E. A. *et al.* Tracking whole-brain connectivity dynamics in the resting state. *Cerebral Cortex* **24**,  
689 663–676 (2012).
- 690 [55] Simony, E. & Chang, C. Analysis of stimulus-induced brain dynamics during naturalistic paradigms.  
691 *NeuroImage* **216**, 116461 (2020).
- 692 [56] Zar, J. H. *Biostatistical analysis* (Prentice-Hall, 2010).
- 693 [57] Tipping, M. E. & Bishop, C. M. Probabilistic principal component analysis. *Journal of Royal Statistical  
694 Society, Series B* **61**, 611–622 (1999).
- 695 [58] Spearman, C. General intelligence, objectively determined and measured. *American Journal of Psychology*  
696 **15**, 201–292 (1904).
- 697 [59] Jutten, C. & Herault, J. Blind separation of sources, part I: an adaptive algorithm based on neuromimetic  
698 architecture. *Signal Processing* **24**, 1–10 (1991).
- 699 [60] Comon, P., Jutten, C. & Herault, J. Blind separation of sources, part II: problems statement. *Signal  
700 Processing* **24**, 11–20 (1991).
- 701 [61] van der Maaten, L. J. P. & Hinton, G. E. Visualizing high-dimensional data using t-SNE. *Journal of  
702 Machine Learning Research* **9**, 2579–2605 (2008).
- 703 [62] McInnes, L., Healy, J. & Melville, J. UMAP: uniform manifold approximation and projection for  
704 dimension reduction. *arXiv* **1802** (2018).
- 705 [63] Lee, D. D. & Seung, H. S. Learning the parts of objects by non-negative matrix factorization. *Nature*  
706 **401**, 788–791 (1999).
- 707 [64] Manning, J. R., Ranganath, R., Norman, K. A. & Blei, D. M. Topographic factor analysis: a Bayesian  
708 model for inferring brain networks from neural data. *PLoS One* **9**, e94914 (2014).
- 709 [65] Gershman, S. J., Blei, D. M., Pereira, F. & Norman, K. A. A topographic latent source model for fMRI  
710 data. *NeuroImage* **57**, 89–100 (2011).
- 711 [66] Mairal, J. B., Bach, F., Ponce, J. & Sapiro, G. Online dictionary learning for sparse coding. *Proceedings  
712 of the International Conference on Machine Learning* 689–696 (2009).
- 713 [67] Mairal, J., Ponce, J., Sapiro, G., Zisserman, A. & Bach, F. R. Supervised dictionary learning. *Advances  
714 in Neural Information Processing Systems* 1033–1040 (2009).

- 715 [68] Hinton, G. E. & Salakhutdinov, R. R. Reducing the dimensionality of data with neural networks. *Science*  
716 **313**, 504–507 (2006).
- 717 [69] Newman, M. E. J. A measure of betweenness centrality based on random walks. *Social Networks* **27**,  
718 39–54 (2005).
- 719 [70] Opsahl, T., Agneessens, F. & Skvoretz, J. Node centrality in weighted networks: generalizing degree  
720 and shortest paths. *Social Networks* **32**, 245–251 (2010).
- 721 [71] Barthélemy, M. Betweenness centrality in large complex networks. *European Physical Journal B* **38**,  
722 163–168 (2004).
- 723 [72] Geisberger, R., Sanders, P. & Schultes, D. Better approximation of betweenness centrality. *Proceedings  
724 of the Meeting on Algorithm Engineering and Experiments* 90–100 (2008).
- 725 [73] Freeman, L. C. A set of measures of centrality based on betweenness. *Sociometry* **40**, 35–41 (1977).
- 726 [74] Rao, C. R. Diversity and dissimilarity coefficients: a unified approach. *Theoretical Population Biology* **21**,  
727 24–43 (1982).
- 728 [75] Lin, J. Divergence measures based on the Shannon entropy. *IEEE Transactions on Information Theory* **37**,  
729 145–151 (2009).
- 730 [76] Ricotta, C. & Szeidl, L. Towards a unifying approach to diversity measures: bridging the gap between  
731 the Shannon entropy and Rao’s quadratic index. *Theoretical Population Biology* **70**, 237–243 (2006).
- 732 [77] Newman, M. E. J. The mathematics of networks. *The New Palgrave Encyclopedia of Economics* **2**, 1–12  
733 (2008).
- 734 [78] Bonacich, P. Some unique properties of eigenvector centrality. *Social Networks* **29**, 555–564 (2007).
- 735 [79] Lohmann, G. *et al.* Eigenvector centrality mapping for analyzing connectivity patterns in fMRI data of  
736 the human brain. *PLoS One* **5**, e10232 (2010).
- 737 [80] Halu, A., Mondragón, R. J., Panzarasa, P. & Bianconi, G. Multiplex PageRank. *PLoS One* **8**, e78293  
738 (2013).
- 739 [81] Honey, C. J., Kötter, R., Breakspear, M. & Sporns, O. Network structure of cerebral cortex shapes  
740 functional connectivity on multiple time scales. *Proceedings of the National Academy of Sciences, USA* **104**,  
741 10240–10245 (2007).

- 742 [82] Schreiber, T. Measuring information transfer. *Physical Review Letters* **85**, 461–464 (2000).
- 743 [83] Alvarez-Hamelin, I., Dall'Asta, L., Barrat, A. & Vespignani, A. *k*-corr decomposition: a tool for the  
744 visualization of large scale networks. *arXiv cs/0504107v2* (2005).
- 745 [84] Christakis, N. A. & Fowler, J. H. Social network sensors for early detection of contagious outbreaks.  
746 *PLoS One* **5**, e12948 (2010).
- 747 [85] Rubinov, M. & Sporns, O. Complex network measures of brain connectivity: uses and interpretations.  
748 *NeuroImage* **52**, 1059–1069 (2010).
- 749 [86] Estrada, E. & Rodríguez-Velázquez, J. A. Subgraph centrality in complex networks. *Physical Review E*  
750 **71**, 056103 (2005).
- 751 [87] Thompson, W. H., Richter, C. G., Plavén-Sigray, P. & Fransson, P. Simulations to benchmark time-  
752 varying connectivity methods for fMRI. *PLoS Computational Biology* **14**, e1006196 (2018).
- 753 [88] Capota, M. *et al.* Brain imaging analysis kit (2017).
- 754 [89] Nocedal, J. & Wright, S. J. *Numerical optimization* (Springer, New York, NY, 2006).
- 755 [90] Combrisson, E. *et al.* Visbrain: a multi-purpose GPU-accelerated open-source suite for multimodal  
756 brain data visualization. *Frontiers in Neuroinformatics* **13**, 1–14 (2019).

757 **Figures**

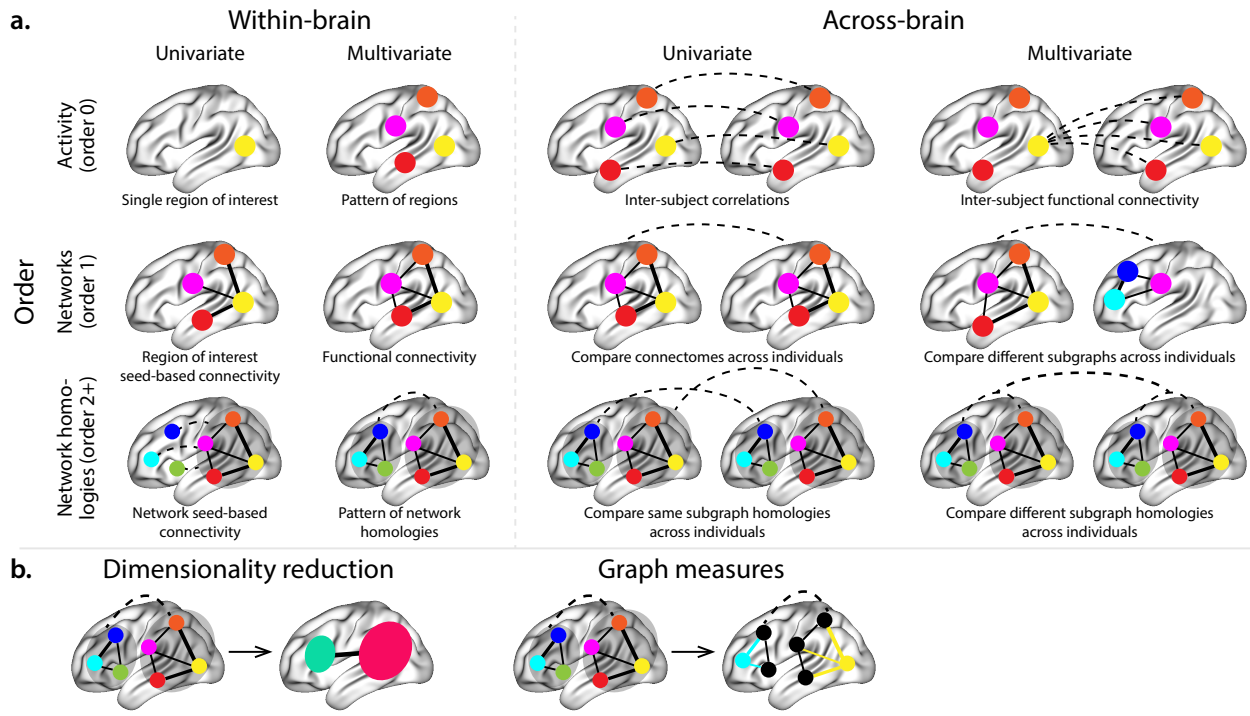


**Figure 1: Neural patterns. a. A space of neural features.** Within-brain analyses are carried out within a single brain, whereas across-brain analyses compare neural patterns across two or more individuals' brains. Univariate analyses characterize the activities of individual units (e.g., nodes, small networks, hierarchies of networks, etc.), whereas multivariate analyses characterize the patterns of activity across units. Order 0 patterns involve individual nodes; order 1 patterns involve node-node interactions; order 2 (and higher) patterns relate to interactions between homologous networks. Each of these patterns may be static (e.g., averaging over time) or dynamic. **b. Summarizing neural patterns.** To efficiently compute with complex neural patterns, it can be useful to characterize the patterns using summary measures. Dimensionality reduction algorithms project the patterns onto lower-dimensional spaces whose dimensions reflect weighted combinations or non-linear transformations of the dimensions in the original space. Graph measures characterize each unit's participation in its associated network.

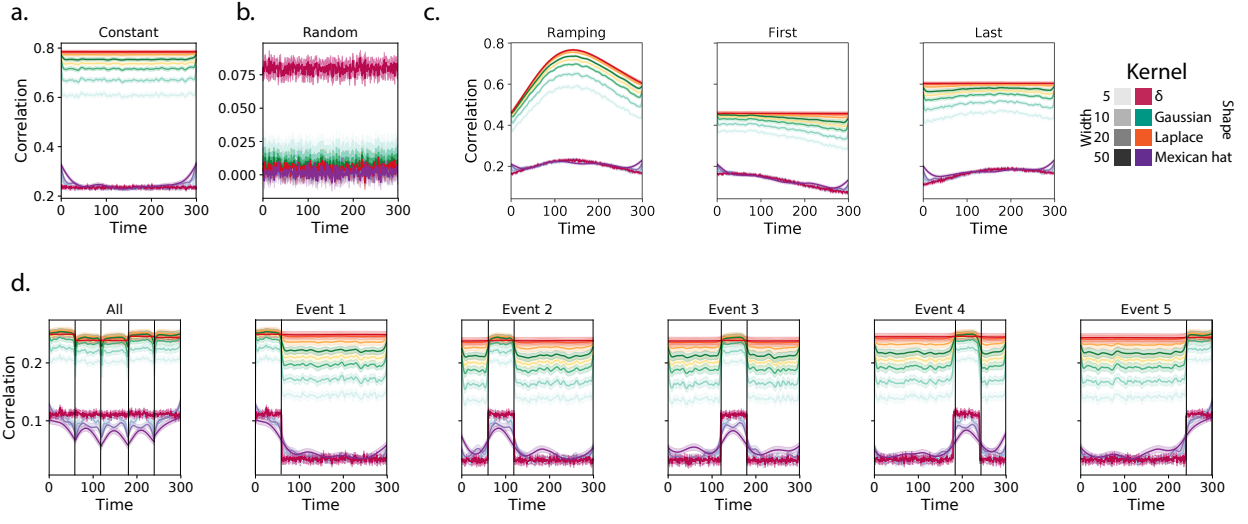


**Figure 2: Recovering known dynamic first-order correlations from synthetic data.** Each panel displays the average correlations between the vectorized upper triangles of the recovered correlation matrix at each timepoint and either the true underlying correlation at each timepoint or a reference correlation matrix. (The averages are taken across 100 different randomly generated synthetic datasets of the given category.) Error ribbons denote 95% confidence intervals (taken across datasets). Different colors denote different kernel shapes, and the shading within each color family denotes the kernel width parameter. For a complete description of each synthetic dataset, see Synthetic data: simulating dynamic first-order correlations. **a. Constant correlations.** These datasets have a stable (unchanging) underlying correlation matrix. **b. Random correlations.** These datasets are generated using a new independently drawn correlation matrix at each new timepoint. **c. Ramping correlations.** These datasets are generated by smoothly varying the underlying correlations between the randomly drawn correlation matrices at the first and last timepoints. The left panel displays the correlations between the recovered dynamic correlations and the underlying ground truth correlations. The middle panel compares the recovered correlations with the first timepoint's correlation matrix. The right panel compares the recovered correlations with the last timepoint's correlation matrix. **d. Event-based correlations.** These datasets are each generated using five randomly drawn correlation matrices that each remain stable for a fifth of the total timecourse. The left panel displays the correlations between the recovered dynamic correlations and the underlying ground truth correlations. The right panels compare the recovered correlations with the correlation matrices unique to each event. The vertical lines denote event boundaries.

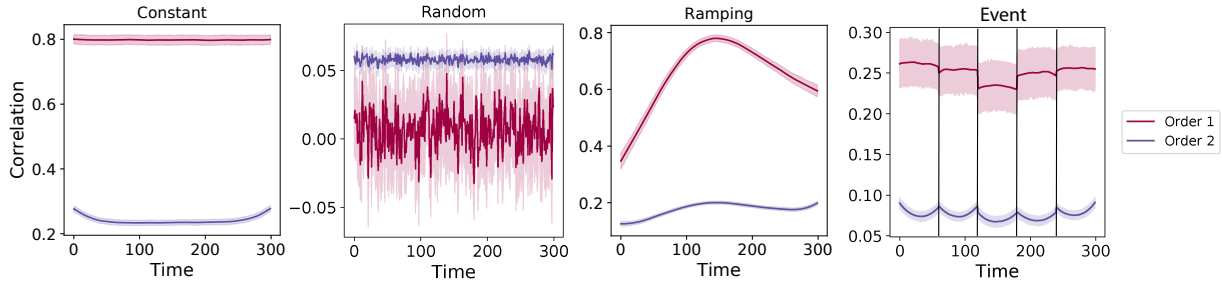


**Figure 3: Recovery of simulated first-order and second-order dynamic correlations.** Each panel displays the average correlations between the vectorized upper triangles of the recovered first-order and second-order correlation matrices and the true (simulated) first-order and second order correlation matrices at each timepoint and for each synthetic dataset. (The averages are taken across 100 different randomly generated synthetic datasets of the given category.) Error ribbons denote 95% confidence intervals (taken across datasets). For a complete description of each synthetic dataset, see Synthetic data: simulating dynamic higher-order correlations. All estimates represented in this figure were computed using a Laplace kernel (width = 20). **Constant.** These datasets have stable (unchanging) underlying second-order correlation matrices. **Random.** These datasets are generated using a new independently drawn second-order correlation matrix at each timepoint. **Ramping.** These datasets are generated by smoothly varying the underlying second-order correlations between the randomly drawn correlation matrices at the first and last timepoints. **Event.** These datasets are each generated using five randomly drawn second-order correlation matrices that each remain stable for a fifth of the total timecourse. The vertical lines denote event boundaries. Note that the “dips” and “ramps” at the boundaries of sharp transitions (e.g., the beginning and ends of the “constant” and “ramping” datasets, and at the event boundaries of the “event” datasets) are finite-sample effects that reflect the reduced numbers of samples that may be used to accurately estimate correlations at sharp boundaries.

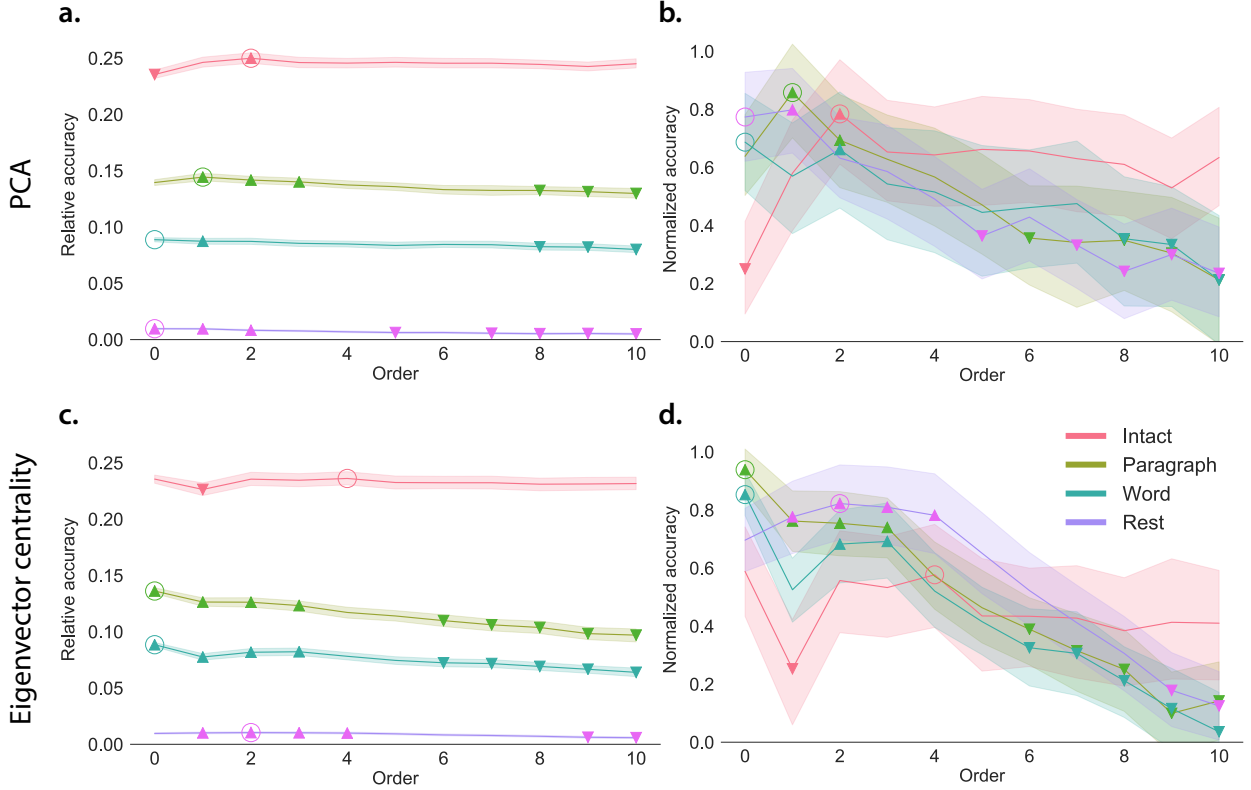


**Figure 4: Across-participant timepoint decoding accuracy varies with correlation order and cognitive engagement.**

**a. Decoding accuracy as a function of order: PCA.** Order ( $x$ -axis) refers to the maximum order of dynamic correlations that were available to the classifiers (see Feature weighting and testing). The reported across-participant decoding accuracies are averaged over all kernel shapes and widths (see Identifying robust decoding results). The  $y$ -values are displayed relative to chance accuracy (intact:  $\frac{1}{300}$ ; paragraph:  $\frac{1}{272}$ ; word:  $\frac{1}{300}$ ; rest:  $\frac{1}{400}$ ; these chance accuracies were subtracted from the observed accuracies to obtain the relative accuracies reported on the  $y$ -axis). The error ribbons denote 95% confidence intervals across cross-validation folds (i.e., random assignments of participants to the training and test sets). The colors denote the experimental condition. Arrows denote sets of features that yielded reliably higher (upward facing) or lower (downward facing) decoding accuracy than the mean of all other features (via a two-tailed  $t$ -test, thresholded at  $p < 0.05$ ). Figure 5 displays additional comparisons between the decoding accuracies achieved using different sets of neural features. The circled values represent the maximum decoding accuracy within each experimental condition.

**b. Normalized timepoint decoding accuracy as a function of order: PCA.** This panel displays the same results as Panel a, but here each curve has been normalized to have a maximum value of 1 and a minimum value of 0 (including the upper and lower bounds of the respective 95% confidence intervals). Panels a and b used PCA to project each high-dimensional pattern of dynamic correlations onto a lower-dimensional space.

**c. Timepoint decoding accuracy as a function of order: eigenvector centrality.** This panel is in the same format as Panel a, but here eigenvector centrality has been used to project the high-dimensional patterns of dynamic correlations onto a lower-dimensional space.

**d. Normalized timepoint decoding accuracy as a function of order: eigenvector centrality.** This panel is in the same format as Panel b, but here eigenvector centrality has been used to project the high-dimensional patterns of dynamic correlations onto a lower-dimensional space. See Figures S1 and S2 for decoding results broken down by kernel shape and width, respectively.

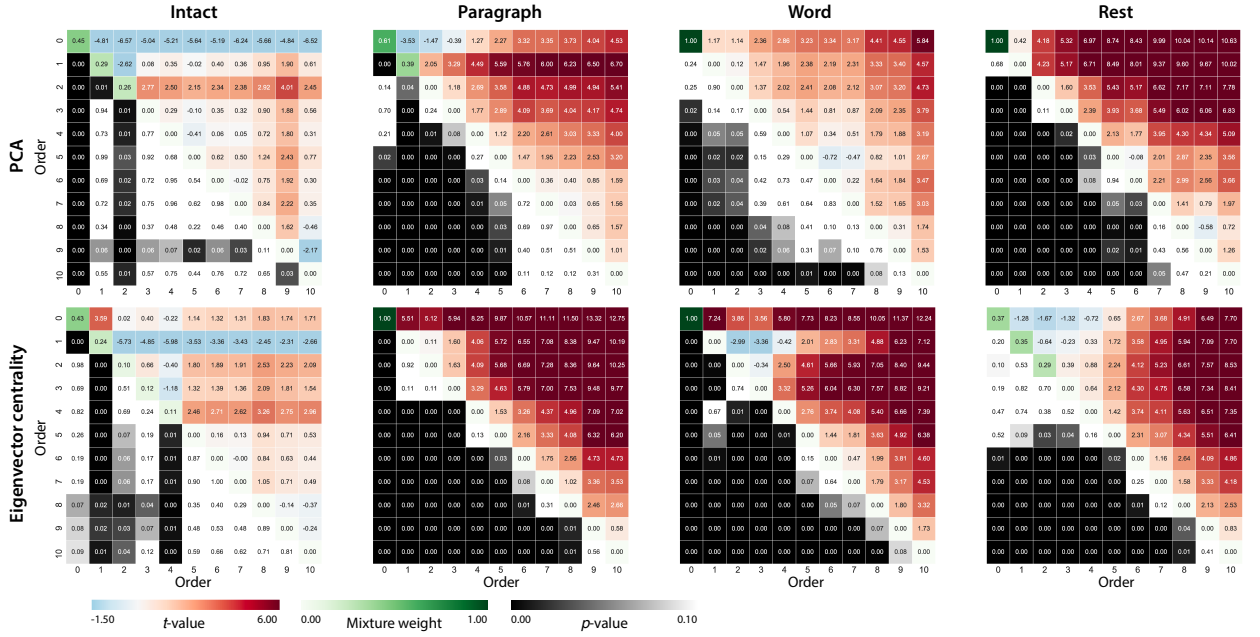


**Figure 5: Statistical summary of decoding accuracies for different neural features.** Each column of matrices displays decoding results for one experimental condition (intact, paragraph, word, and rest). We considered dynamic activity patterns (order 0) and dynamic correlations at different orders (order > 0). We used two-tailed  $t$ -tests to compare the distributions of decoding accuracies obtained using each pair of features. The distributions for each feature reflect the set of average decoding accuracies (across all kernel parameters), obtained for each random assignment of training and test groups. In the upper triangles of each matrix, warmer colors (positive  $t$ -values) indicate that the neural feature indicated in the given row yielded higher accuracy than the feature indicated in the given column. Cooler colors (negative  $t$ -values) indicate that the feature in the given row yielded lower decoding accuracy than the feature in the given column. The lower triangles of each map denote the corresponding  $p$ -values for the  $t$ -tests. The diagonal entries display the relative average optimized weight given to each type of feature in a decoder that included all feature types (see Feature weighting and testing).

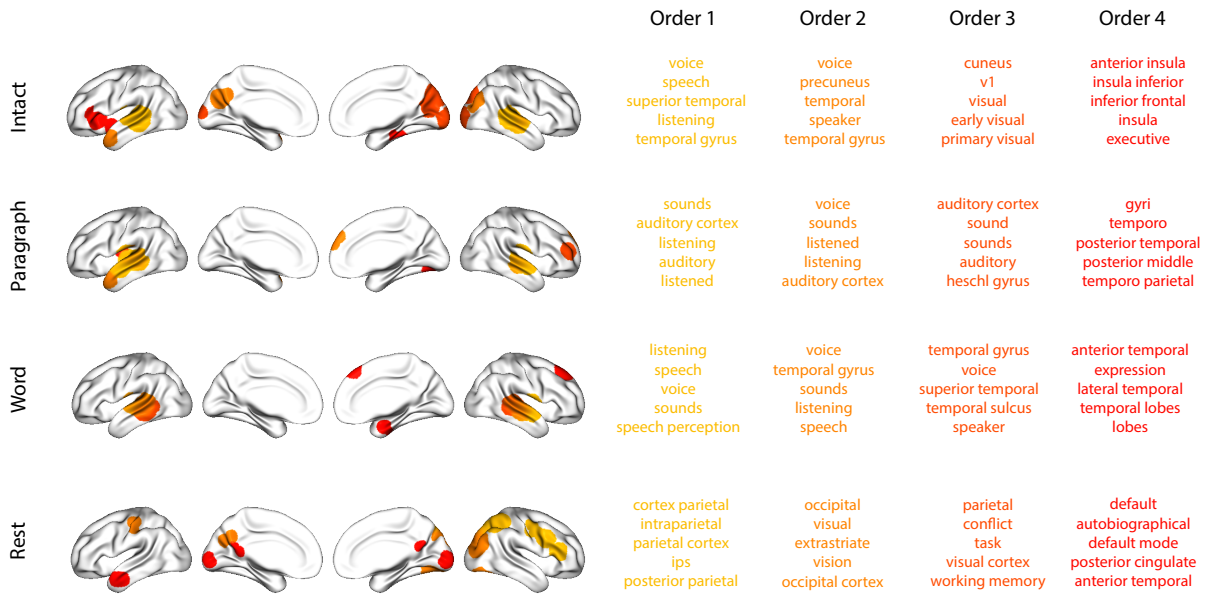


**Figure 6: Top terms associated with the most strongly correlated nodes at each order.** Each color corresponds to one order of inter-subject functional correlations. To calculate the dynamic correlations, eigenvector centrality has been used to project the high-dimensional patterns of dynamic correlations onto a lower-dimensional space at each previous order, which allows us to map the brain regions at each order by retaining the features of the original space. The inflated brain plots display the locations of the endpoints of the 10 strongest (absolute value) correlations at each order, thresholded at 0.999, and projected onto the cortical surface<sup>90</sup>. The lists of terms on the right display the top five Neurosynth terms<sup>38</sup> decoded from the corresponding brain maps for each order. Each row displays data from a different experimental condition. Additional maps and their corresponding Neurosynth terms may be found in the Supplementary materials (intact: Fig. S5; paragraph: Fig. S6; word: Fig. S7; rest: Fig. S8).

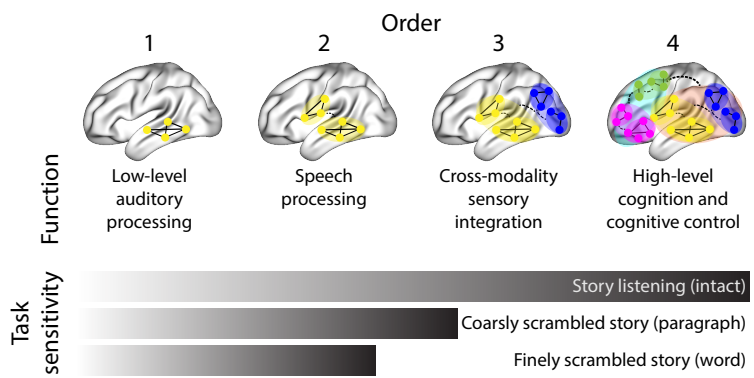


**Figure 7: Proposed high-order network dynamics underlying high-level cognition during story listening.** Schematic depicts higher orders of network interactions supporting higher-level aspects of cognitive processing. When tasks evoke richer, deeper, and/or higher-level processing, this is reflected in higher-order network interactions.

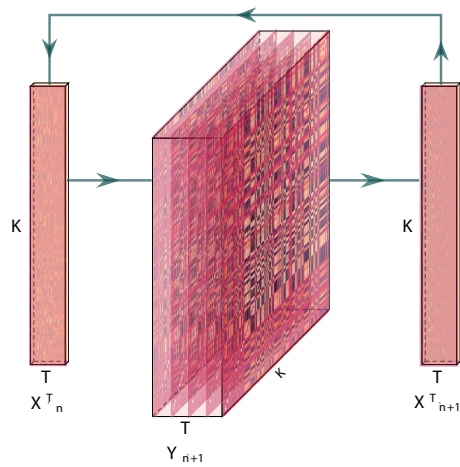


**Figure 8: Estimating dynamic high-order correlations.** Given a  $T$  by  $K$  matrix of multivariate timeseries data,  $\mathbf{X}_n$  (where  $n \in \mathbb{N}, n \geq 0$ ), we use Equation 4 to compute a timeseries of  $K$  by  $K$  correlation matrices,  $\mathbf{Y}_{n+1}$ . We then approximate  $\mathbf{Y}_{n+1}$  with the  $T$  by  $K$  matrix  $\mathbf{X}_{n+1}$ . This process may be repeated to scalably estimate iteratively higher-order correlations in the data. Note that the transposes of  $\mathbf{X}_n$  and  $\mathbf{X}_{n+1}$  are displayed in the figure for compactness.

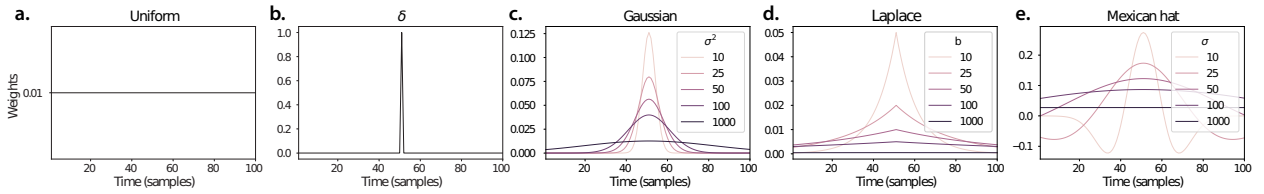


**Figure 9: Examples of kernel functions.** Each panel displays per-timepoint weights for a kernel centered at  $t = 50$ , evaluated at 100 timepoints ( $\tau \in [1, \dots, 100]$ ). **a. Uniform kernel.** The weights are timepoint-invariant; observations at all timepoints are weighted equally, and do not change as a function of  $\tau$ . This is a special case kernel function that reduces dynamic correlations to static correlations. **b. Dirac  $\delta$  kernel.** Only the observation at timepoint  $t$  is given a non-zero weight (of 1). **c. Gaussian kernels.** Each kernel's weights fall off in time according to a Gaussian probability density function centered on time  $t$ . Weights derived using several different example width parameters ( $\sigma^2$ ) are displayed. **d. Laplace kernels.** Each kernel's weights fall off in time according to a Laplace probability density function centered on time  $t$ . Weights derived using several different example width parameters ( $b$ ) are displayed. **e. Mexican hat (Ricker wavelet) kernels.** Each kernel's weights fall off in time according to a Ricker wavelet centered on time  $t$ . This function highlights the contrasts between local versus surrounding activity patterns in estimating dynamic correlations. Weights derived using several different example width parameters ( $\sigma$ ) are displayed.

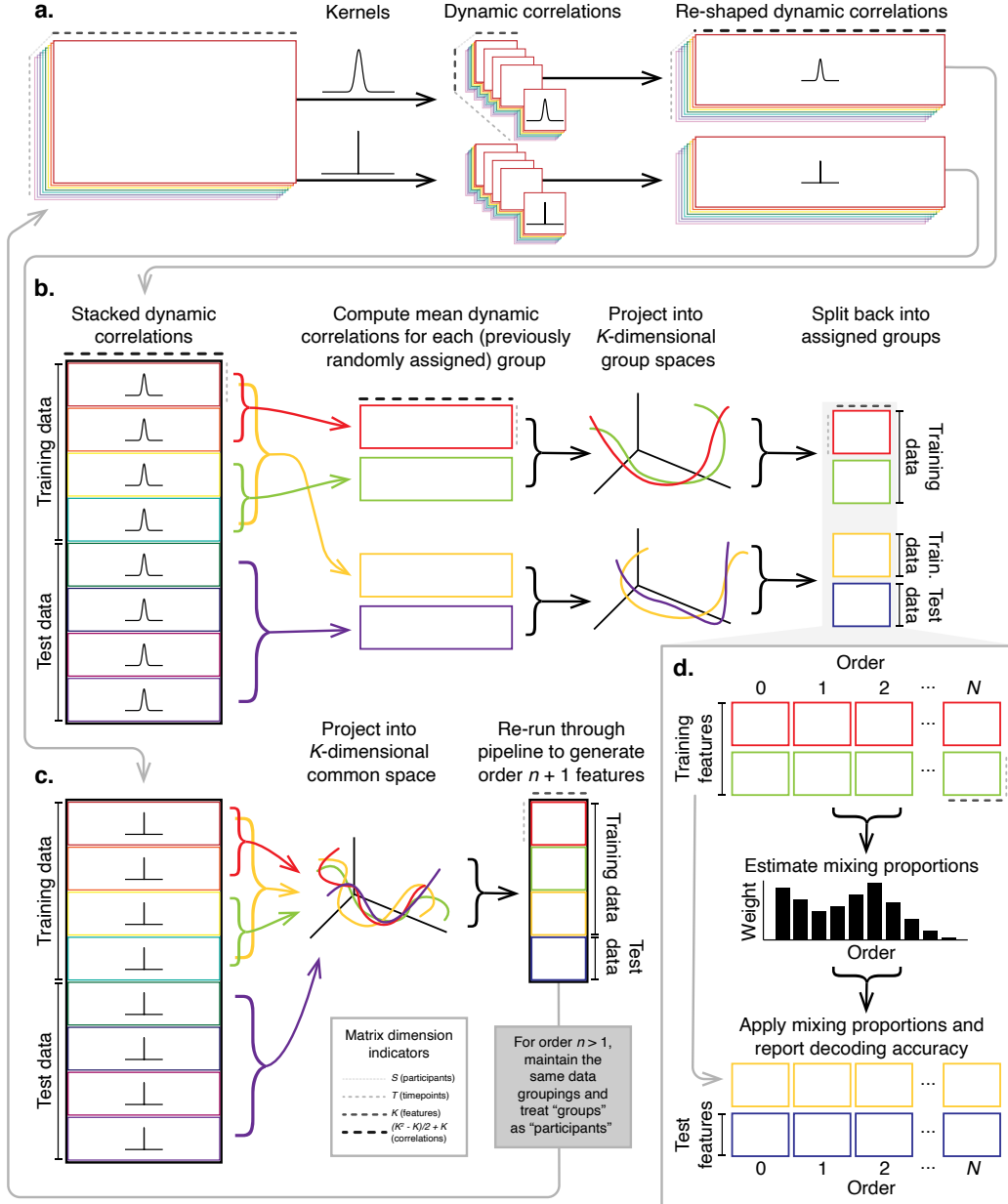


**Figure 10: Decoding analysis pipeline.** **a. Computing dynamic correlations from timeseries data.** Given a timeseries of observations as a  $T \times K$  matrix (or a set of  $S$  such matrices), we use Equation 4 to compute each participant's DISFC (relative to other participants in the training or test sub-group, as appropriate). We repeat this process twice—once using the analysis kernel (shown here as a Gaussian in the upper row of the panel), and once using a  $\delta$  function kernel (lower row of the panel). **b. Projecting dynamic correlations into a lower-dimensional space.** We project the training and test data into  $K$ -dimensional spaces to create compact representations of dynamic correlations at the given order (estimated using the analysis kernel). **c. Kernel trick.** We project the dynamic correlations computed using a  $\delta$  function kernel into a common  $K$ -dimensional space. These low-dimensional embeddings are fed back through the analysis pipeline in order to compute features at the next-highest order. **d. Decoding analysis.** We split the training data into two equal groups, and optimize the feature weights (i.e., dynamic correlations at each order) to maximize decoding accuracy. We then apply the trained classifier to the (held-out) test data.